Switching dynamics and ultrafast inversion control of quantum dots for on-chip optical information processing

Xun Ma and Sajeev John
Department of Physics, University of Toronto, 60 St. George Street, Toronto, Ontario, Canada M5S 2E4
(Received 7 October 2009; published 4 December 2009)

We demonstrate dynamical near-complete inversion switching of a two-level quantum dot driven by picosecond optical pulses in a bimodal photonic band gap (PBG) waveguide at microwatt power levels. This is enabled by a sharp steplike discontinuity in the local (electromagnetic) density of states (LDOS) provided by a cutoff in one of the two waveguide modes. The atomic Bloch vector equations in this colored vacuum are derived using dressed state description of the atomic density operator in the presence of phonon-mediated dephasing. Instead of assuming phenomenological decay rates, we derive explicit expressions for decay terms of bare state atomic dipole moments and population in the Born-Markov approximation from a master equation approach. Giant Mollow splitting of the atom level due to subwavelength light localization of strong driving pulse causes the time-dependent Mollow bands to straddle the LDOS jump, leading to different radiative decay rates in the upper and lower Mollow sidebands. This results in remarkable field-dependent spontaneous emission and dipolar dephasing rates, combined with a novel "vacuum structure" term in the Bloch equations. Our Bloch equations predict ultrafast high-contrast inversion switching that is activated and deactivated by picosecond pulse trains detuned below and above the atomic resonance, respectively. This dynamic inversion is due to the rapid rise in relaxation rates as the pulse amplitude rises, causing the Bloch vector to switch from antiparallel to parallel alignment with the pulse "torque vector." Subsequent near-complete inversion occurs through an adiabatic following process retained long after the pulse amplitude subsides and the system reverts to slow relaxation. For a 1% inhomogeneously broadened distribution of quantum dot with average of 100 D dipole moment, driven by 1.5 μm picosecond pulses and coupled to a cutoff mode LDOS jump with radiative emission rates of $\gamma_{high}=2.5$ THz and $\gamma_{low}=5$ GHz, a large average population switching contrast of 0.5 is demonstrated with a phonon dephasing rate $\gamma_p=0.5$ THz. A 1.6 fJ control pulse is required per switching operation and a 30 μW pulse train is sufficient to maintain the inversion. This switchable gain (loss) segment of the PBG waveguide can be used to controllably amplify (absorb) signal pulses conveying optical information. This provides a robust mechanism for ultrafast multiwavelength channel all-optical logic in PBG microchips.

DOI: 10.1103/PhysRevA.80.063810 PACS number(s): 42.50.Hz, 42.70.Qs, 32.80.−t, 42.50.Ct

I. INTRODUCTION

Based on the properties of light localization [1,2] and inhibited spontaneous emission [3], photonic band gap (PBG) materials have emerged as a broad and robust platform for integrated photonics. These photonic crystals (PCs) modify the dispersion relations of electromagnetic waves, thereby changing the vacuum electromagnetic density of states (DOS) throughout an extended volume of the material. Electromagnetic waves with a frequency within the photonic band gap cannot propagate inside the crystal but may be confined within subwavelength regions with lifetimes limited only by absorption or nonlinear decay processes. Guiding of light through subwavelength scale circuit paths [4–8] enables very strong optical fields at very low power levels for exceptional nonlinear optical effects.

Whereas the PBG is generally regarded as a spectral range in which the electromagnetic DOS vanishes, engineered defects in the otherwise periodic microstructure can have the opposite effect. Waveguide architectures within a three-dimensional (3D) PBG can achieve very large local density of states (LDOS) via mode cutoff, with Purcell factors (ratio of spontaneous emission rate to that in free space) of several thousands [9,10]. In this case, spontaneous emission that would normally occur in nanoseconds can be accelerated to occur in a picosecond, enabling radiative emission to supercede phonon-mediated (nonradiative) relaxation even at room temperature.

In this paper, we theoretically demonstrate dynamic inversion of the quantum-dot population driven by picosecond femtojoule laser pulses in a bimodel PC waveguide with cutoff mode. Nonlinear quantum-dot dynamics in this strong-coupling engineered vacuum was introduced recently [11]. As a result of the LDOS jump, important "vacuum structure terms" in the atomic Bloch vector equation together with field-dependent spontaneous emission and dipolar relaxation rates drastically alter Bloch vector dynamics from that of ordinary vacuum. This forces a rapid realignment of the atomic Bloch vector from antiparallel to parallel to the pulse "torque vector" as the pulse approaches its peak. Subsequent adiabatic following brings the quantum dot to near-complete population inversion that persists after the pulse subsides. The inversion can be maintained by a train of picosecond pulses tuned slightly below the resonance transition frequency. The quantum dot can be switched back to its ground state using a picosecond optical pulse tuned slightly above the resonance transition. This high-contrast dynamic control of the quantum-dot Bloch vector is robust to picosecond time scale phonon dephasing and provides a promising mechanism for nearly terabit per second all-optical logic at micro-

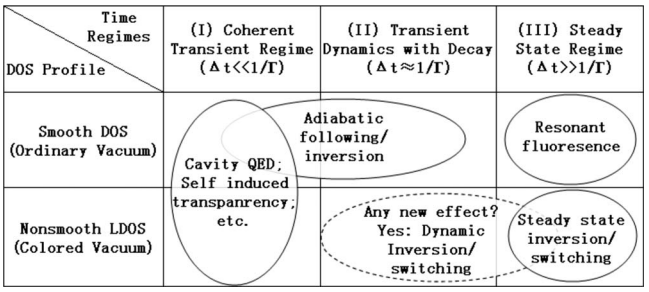

FIG. 1. Distinct interaction regimes for resonance quantum optics. The regime with pulse duration Δ_t comparable with relaxation time $1/\Gamma$ in the colored vacuum contains striking and distinct physics not attainable in other regimes.

watt power level in a photonic band gap microchip.

Resonant quantum optics in the strong coherent coupling regime is a subject of fundamental scientific importance. In this regime, the resonator's coherent coupling to a specific set of photonic modes is much stronger than its coupling to the dissipative environment, so that transient light-matter dynamics occurs much faster than the dissipation due to the environment (electromagnetic or phonon heat bath). In this case, novel quantum mechanical nonlinearities not observed in the classical system may emerge. Previously, strong coupling has been experimentally studied using a dilute gas of two-level atoms, driven resonantly by coherent optical fields or coupled to the resonant mode of planar cavities. However, the realization of strong coupling of a single two-level solid-state system (i.e., a quantum dot) has not been realized until recently [12–17]. The demonstrations of vacuum Rabi splitting [12–14] and Mollow splitting [15–17] inside photonic crystal nanocavities, as well as other semiconductor microcavities, have sparked broad interest in on-chip quantum electrodynamics with important potential applications in single photon sources and quantum information processing.

Resonance light-matter system can occur in either (A) smooth electromagnetic DOS such as free space or (B) discontinuous LDOS inside photonic crystals. The electromagnetic vacuum influences the light-matter interaction through radiative relaxation of the atomic dipole and population. According to the length of interaction time scale Δ_t (e.g., pulse duration, observation time, etc.) relative to the relaxation time scale $1/\Gamma$, three time regimes can be identified (Fig. 1). In (I) the coherent transient regime $\Delta_t \ll 1/\Gamma$, the amount of relaxation during the interaction can be ignored and only the transient light-matter dynamics needs to be considered. Vacuum Rabi oscillations [18,19] and self-induced transparency [19,20] belong to this regime, as well as adiabatic following and adiabatic inversion in ordinary vacuum [19,21,22]. In regime (II), $\Delta_t \sim 1/\Gamma$, both the transient dynamics and the dissipation need to be taken into account. The adiabatic following and inversion can still exist in this regime, although influenced by dissipation. In the long interaction regime (III), $\Delta_t \gg 1/\Gamma$, dissipation has enough time to bring the system to a stationary steady state so that only long time behavior is important. Resonant fluorescence is a good example [23].

Photonic crystals provide a novel platform for studying near resonant light-matter interactions. Strong coupling is achievable inside photonic crystals due to field enhancement effects [24] and strong suppression of the electromagnetic vacuum DOS deep inside the photonic band gap. The recent realization of quantum-dot vacuum Rabi splitting [12] utilizes the first feature. Important effects of the reduced DOS on light-matter interactions include the photon-atom bound state [25] and localization of super-radiance [26]. The DOS, albeit strongly suppressed, may be smooth and featureless deep inside the gap, as in ordinary vacuum. Even with the presence of a nonsmooth DOS profile (e.g., waveguide cutoff mode), the dynamics in the coherent transient time regime are not significantly affected since the amount of dissipation can be ignored and the system does not have enough time to fully sense the vacuum structure. The same phenomena as in a smooth DOS environment (ordinary vacuum) with possible enhancements are expected to occupy the bottom left region in Fig. 1.

On the other hand, as the interaction time increases, a discontinuous LDOS allows relaxation to play a much richer role during the resonant light-matter interaction. This leads to new phenomena not observed in a smooth DOS environment. In particular, steady-state population inversion and switching of two-level systems controlled by an external continuous wave (cw) have been demonstrated [27–29]. This phenomenon belongs to the bottom right region in the table of Fig. 1. However, the $\Delta_t \sim 1/\Gamma$ region with a nonsmooth LDOS profile in Fig. 1 is still unexplored. It is the aim of this paper to delineate striking and unexpected phenomena resulting from resonant light-matter interactions in this region.

Driven two-level quantum systems in ordinary vacuum have a long and rich history [19]. The optical Bloch equation is a standard tool to describe the evolution of atomic dipole moments and population, driven by a coherent laser beam. Spontaneous emission in ordinary vacuum is described by fixed exponential decay in the Markov approximation [19]. Near a photonic band edge, however, the vacuum LDOS may vary significantly within a very small frequency range. This leads to memory effects not captured in the Markov description. However, if the LDOS variations are confined to an infinitesimal frequency range (sharp jump) and the LDOS is smooth elsewhere, a Markov approximation can be applied locally for frequencies away from the immediate vicinity of the sharp jump [27,30]. Provided that all atomic Mollow bands associated with strong-field resonance fluorescence avoid the sharp LDOS jump, a master equation for the dressed atom can be derived in a local Markov approximation when driven by a cw laser field. In this context, weak steady-state population inversion of a single atom has been demonstrated [27,31–33] as well as enhanced steady-state collective atomic inversion [30]. It has also been shown [28] that non-Markovian effects from the band edge serve to lower the population switching threshold and to improve the switching sharpness and contrast.

In this paper, we extend the dressed state master equation formalism for a cw laser beam in [27] into a time-dependent driving beam (laser pulses). We derive the Bloch vector equation and we demonstrate how this fundamental equation is qualitatively modified by electromagnetic vacuum structure. We study a two-level system (e.g., a quantum dot) driven by strong laser pulses near a one-dimensional photo-

nic band edge provided by a waveguide cutoff mode within a 3D PBG material. This leads to a generalization of the Bloch equation that accommodates the structure of the LDOS jump into the spontaneous emission terms. Unlike the stationary dressed states of a cw beam [27], the pulse-driven dressed states are strongly time-dependent and the true Bloch vector differs considerably from the corresponding instantaneous steady-state Bloch vector (the long term equilibrium state of the Bloch vector if the field strength was to remain at the current value for a long enough time). Unlike ordinary vacuum, the relaxation rates of the atomic Bloch vector components toward the instantaneous steady-state Bloch vector are strongly field dependent. This leads to rapid attraction of the Bloch vector toward a weakly inverted state during the peak of the incident optical pulse. This rapid attraction is characterized by subpicosecond realignment of the Bloch vector from antiparallel to parallel orientation with respect to the pulse torque vector. As the pulse subsides, the instantaneous steady-state Bloch vector reverts to its ground state configuration. However the field-dependent relaxation rates become much slower and the true atomic Bloch vector remains in an inverted state. Moreover, this Bloch vector adiabatically follows the orientation of the pulse torque vector and achieves a nearly completely inverted state that persists long after the pulse has subsided. This highly inverted state can be maintained by a train of picosecond "control pulses." An inhomogeneously broadened collection of inverted quantum dots in this photonic band gap waveguide can then act as a strong gain medium for incoming signal pulses in various wavelength channels. The gain medium can be coherently switched back to an absorbing medium by means of a control pulse that is detuned slightly above the inhomogeneously broadened atomic distribution. This ultrafast coherently switchable waveguide segment can then be used to perform optical logic operations on signal pulses passing through the same segment in various wavelength channels.

Adiabatic population inversion of two-level atoms through laser pulses has previously been achieved in ordinary vacuum through various forms of frequency chirping during the passage of the laser pulse [19,21,22,34–39]. Examples include tuning the atomic gas transition frequency via Stark shift [22], laser frequency sweeping [35,36], self-phase modulation [37], and intrinsic frequency chirping of dense two-level systems through resonant dipole-dipole interactions [38,39]. Our dynamic switching through electromagnetic vacuum structure also utilizes an adiabatic following process but does not require any form of the frequency chirping or phase modulation techniques. The role of frequency chirping is now replaced by the vacuum structure that forces realignment of the atomic Bloch vector with the pulse torque vector during the steady-state attraction process. This simplification of the inversion process enables a broader range of control and simpler signal pulses in the operation of an on-chip optical microtransistor.

In Sec. II, we give a detailed derivation of the master equation in the time-dependent dressed state basis and interaction picture under Born-Markov approximations. The master equation is then transferred back into the bare atomic basis and Schrödinger picture. In Sec. III, the master equation is used to obtain the generalized Bloch vector equation with field-dependent relaxation terms and a vacuum structure term. In Sec. IV, we give a detailed study of the steady-state properties of a cw-driven system from the Bloch equation point of view. This recaptures and generalizes earlier results [27]. In Sec. V, we demonstrate the dynamical switching mechanism of a quantum dot from the dynamical evolution of the atomic Bloch vector. We elucidate the steady-state attraction and adiabatic conditions required for the optical pulse in Sec. V A. Finally, in Sec. VI, we discuss the possibility of applying the dynamical switching phenomena to ultrafast all-optical switches. We propose a model device composed of two channels of picosecond pulses controlling the population inversion of a collection of inhomogeneously broadened but independent two-level quantum dots near a photonic band edge. A population switching contrast up to 0.5 is achieved in the presence of picosecond time scale phonon dephasing. The switched two-level medium is then capable of controlling the propagation of subsequent resonant signal pulses. This shows the possibility of realizing on-chip ultrafast all-optical switches via modified atom Bloch vector dynamics in a structured electromagnetic vacuum.

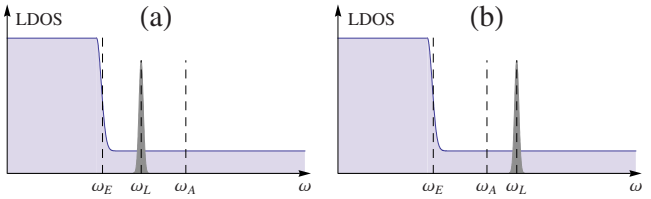

FIG. 2. (Color online) The step-shaped LDOS model with a band-edge frequency ω_E. This is provided by a bimodal waveguide in a 3D PBG material, in which one of the waveguide modes has a cutoff at ω_E [9,33]. The quantum-dot (atomic) transition frequency ω_A and the pulse central frequency ω_L are in the low LDOS region. Two possible atom-field detunings are shown, with (a) $\Delta_{AL}>0$ and (b) $\Delta_{AL}<0$.

II. MASTER EQUATION FOR QUANTUM-DOT DENSITY MATRIX

We consider a two-level atom with transition frequency ω_A detuned slightly from a step discontinuity in the electromagnetic density of states at frequency ω_E (Fig. 2), interacting with a laser pulse $E(t)$ with central frequency ω_L and envelop function $\mathcal{E}(t)$. The step-shaped electromagnetic DOS can be provided by a waveguide cutoff mode within a 3D-two-dimensional (2D) PGB heterostructure [9]. The atom also interacts with a smooth featureless nonradiative reservoir that is statistically independent from the photonic reservoir. This coupling to phonons causes dephasing of the atomic dipole. The contributions of the two reservoirs to the reduced master equation are assumed to factorize and can be treated separately. The contribution of the phonon reservoir to the master equation is described elsewhere [27]. We focus here on the derivation of the radiative part of the master equation.

We consider a classical optical pulse with electric field amplitude,

$$E(t) = \mathcal{E}(t)\cos(\omega_L t). \tag{1}$$

The Hamiltonian, in the absence of phonon coupling, consists of three parts,

$$H = H_S + H_R + H_{SR}. \tag{2}$$

H_S is the Hamiltonian of the pulse-driven atom, H_R describes the electromagnetic reservoir, H_{SR} is the atom-reservoir coupling. In the bare atomic basis (ground state $|1\rangle$ and excited state $|2\rangle$), this Hamiltonian (in the rotating wave approximation in rotating frame ω_L) takes the form [27]

$$H_S = \tfrac{1}{2}\hbar\Delta_{AL}\sigma_3 - \hbar\epsilon(t)(\sigma_{21} + \sigma_{12}),$$

$$H_R = \sum_\lambda \hbar\omega_\lambda a_\lambda^\dagger a_\lambda,$$

$$H_{SR} = i\hbar\sum_\lambda g_\lambda(a_\lambda^\dagger\sigma_{12} - a_\lambda\sigma_{21}). \tag{3}$$

Here the time-dependent Rabi frequency $\epsilon(t)=d_{21}|\mathcal{E}(t)|/\hbar$ and $\mathbf{d_{21}}$ is the quantum-dot dipole transition matrix element. We assume $|\mathbf{d_{12}}|=|\mathbf{d_{21}}|=d_{21}$, $\mathcal{E}(t)=\mathcal{E}(t)^*$, and that the dipole is parallel to the pulse polarization for simplicity. $a_\lambda^\dagger$ and a_λ are the creation and annihilation operators of mode λ of the electromagnetic reservoir with frequency ω_λ. We define the bare atomic operators $\sigma_{ij}=|i\rangle\langle j|$ $(i,j=1,2)$, population inversion $\sigma_3=\sigma_{22}-\sigma_{11}$, the detunings $\Delta_{AL}=\omega_A-\omega_L$, and $\Delta_\lambda=\omega_\lambda-\omega_L$.

Due to the large transition dipole moment of semiconductor quantum dots (typically 10–100 times larger than natural atoms) and strong light localization within 3D PBG defect structures, it is possible to achieve orders of magnitude larger Rabi frequencies and Mollow splitting than those in free space. The mode volume of photonic crystal cavities is typically smaller than the cubic wavelength $V_{eff}<(\lambda/n)^3$ [12,40,41], with λ being the vacuum wavelength and n being the refractive index of the dielectric material composing the photonic crystal structure. If we consider the energy of one photon at $\lambda\approx 1.5$ μm to be evenly distributed within the cavity with $V_{eff}\sim(\lambda/n)^3$ or smaller, then the average field strength is on the order of $E_{avg}\sim 10^3$–10^4 V/cm (assume $n=1$). This corresponds to vacuum Rabi splitting on the order of 100 μeV–1 meV for a typical quantum-dot dipole moment $d_{21}\sim 10^{28}$ C m. In fact, 100 μeV size vacuum Rabi splittings have been widely observed [12–14] and 1 meV Rabi splitting has been predicted [42] for a single quantum dot inside PBG and other semiconductor microcavities. For a quantum dot driven by a coherent laser field, the resulting Mollow splitting is proportional to the square root of photon number, so 10^2 photons would be enough to induce a resonant Mollow splitting that is ten times the vacuum splitting above, or 1–10 meV.

Our estimate above is relatively conservative. For 3D PBG cavities, mode volumes of $0.2(\lambda/n)^3$ are possible [43], leading to even stronger fields, and the dipole moments of quantum dots can be larger than the value we used above. Furthermore, the Mollow splitting is larger for nonzero frequency detuning Δ_{AL}. As a result, 10 THz (1THz corresponds to about 4 meV of splitting) of Rabi frequency and Mollow splitting are theoretically achievable in 3D PBG waveguides, enabling enough bandwidth for our model to handle picosecond laser pulses in multiple wavelength channels.

A. Time-dependent dressed states

We consider the atom to be dressed by the intense pulse, resulting in the time-dependent dressed states $|\tilde{1}\rangle$ and $|\tilde{2}\rangle$,

$$|\tilde{1}\rangle = c(t)|1\rangle + s(t)|2\rangle,$$

$$|\tilde{2}\rangle = -s(t)|1\rangle + c(t)|2\rangle, \tag{4}$$

where

$$c^2(t) = \{1 + \Delta_{AL}/[2\Omega(t)]\}/2,$$

$$s^2(t) = \{1 - \Delta_{AL}/[2\Omega(t)]\}/2,$$

$$\Omega(t) = [(\Delta_{AL}/2)^2 + \epsilon(t)^2]^{1/2}. \tag{5}$$

Note that c and s should have the same sign. The dressed state atomic operators are defined similarly as their bare state counterparts,

$$\tilde{R}_{ij} = |\tilde{i}\rangle\langle\tilde{j}| \quad (i,j=1,2),$$

$$\tilde{R}_3 = \tilde{R}_{22} - \tilde{R}_{11}.$$

The basis transformation [Eq. (4)] defines a time-dependent unitary operator B that transforms the wave function $|\psi\rangle$ and a general operator O in the bare atomic basis into the dressed atomic basis as $|\tilde{\psi}\rangle=B|\psi\rangle$ and $\tilde{O}=BOB^\dagger$. After this basis transformation, Hamiltonian (2) becomes [44,45]

$$\begin{aligned}\tilde{H} &= BHB^\dagger - i\hbar B\dot{B}^\dagger = \hbar\Omega(t)\tilde{R}_3 + \sum_\lambda \hbar\omega_\lambda a_\lambda^\dagger a_\lambda \\ &+ \sum_\lambda \{i\hbar g_\lambda a_\lambda^\dagger[-c(t)s(t)\tilde{R}_3 + c^2(t)\tilde{R}_{12} - s^2(t)\tilde{R}_{21}] + \text{H.c.}\} \\ &- i\hbar B\dot{B}^\dagger = \tilde{H}_0 + \tilde{H}_i,\end{aligned} \tag{6}$$

with $\tilde{H}_0=\hbar\Omega(t)\tilde{R}_3+\Sigma_\lambda \hbar\omega_\lambda a_\lambda^\dagger a_\lambda$. Then by further transforming to the interaction picture via the unitary operator $U \equiv e^{i\tilde{H}_0(t-t_0)/\hbar}$, the Hamiltonian becomes

$$\begin{aligned}\tilde{H}_I &= U\tilde{H}_i U^\dagger = (i\hbar\sum_\lambda g_\lambda\{a_\lambda^\dagger[-c(t)s(t)\tilde{R}_3 e^{i\Delta_\lambda t} \\ &+ c^2(t)\tilde{R}_{12}e^{i[\Delta_\lambda - 2\Omega(t)]t} - s^2(t)\tilde{R}_{21}e^{i[\Delta_\lambda+2\Omega(t)]t}]\} + \text{H.c.}) \\ &- i\hbar UB\dot{B}^\dagger U^\dagger = \tilde{H}_{SR}^I(t) - i\hbar UB\dot{B}^\dagger U^\dagger.\end{aligned} \tag{7}$$

For convenience, we rewrite $\tilde{H}_{SR}^I=\Sigma_{i=1}^6 \tilde{S}_i\tilde{\Gamma}_i$, where

$$\tilde{S}_1 = \tilde{S}_4 = \tilde{R}_3, \quad \tilde{S}_2 = \tilde{S}_5 = \tilde{R}_{12}, \quad \tilde{S}_3 = \tilde{S}_6 = \tilde{R}_{21},$$

$$\tilde{\Gamma}_1 = \tilde{\Gamma}_4^\dagger = -i\hbar\sum_\lambda g_\lambda a_\lambda^\dagger c(t)s(t)e^{i\Delta_\lambda t},$$

$$\tilde{\Gamma}_2 = \tilde{\Gamma}_5^\dagger = i\hbar\sum_\lambda g_\lambda a_\lambda^\dagger c^2(t)e^{i[\Delta_\lambda - 2\Omega(t)]t},$$

$$\tilde{\Gamma}_3 = \tilde{\Gamma}_6^\dagger = -i\hbar \sum_\lambda g_\lambda a_\lambda^\dagger s^2(t) e^{i[\Delta_\lambda + 2\Omega(t)]t}. \tag{8}$$

B. Derivation of the master equation

The density operator of the whole system and reservoir $\tilde{\chi}_I$ obeys the Schrödinger equation

$$\dot{\tilde{\chi}}_I(t) = \frac{1}{i\hbar}[\tilde{H}_I, \tilde{\chi}_I(t)] = \frac{1}{i\hbar}[\tilde{H}_{SR}^I, \tilde{\chi}_I(t)] - [UB\dot{B}^\dagger U^\dagger, \tilde{\chi}_I(t)]. \tag{9}$$

The master equation for the reduced atomic density operator in the Born approximation has the form (see Appendix A for details)

$$\dot{\tilde{\varrho}}_I = [\dot{\tilde{\varrho}}_I]_1 - \mathrm{Tr}_R[UB\dot{B}^\dagger U^\dagger(t), \tilde{\chi}_I(t)] \tag{10}$$

with

$$[\dot{\tilde{\varrho}}_I]_1 = -\sum_{i,j} \frac{1}{\hbar^2} \int_0^t dt' \{[\tilde{S}_i \tilde{S}_j \tilde{\varrho}_I(t) - \tilde{S}_j \tilde{\varrho}_I(t) \tilde{S}_i] \langle \tilde{\Gamma}_i(t) \tilde{\Gamma}_j(t') \rangle_R + [\tilde{\varrho}_I(t) \tilde{S}_j \tilde{S}_i - \tilde{S}_i \tilde{\varrho}_I(t) \tilde{S}_j] \langle \tilde{\Gamma}_j(t') \tilde{\Gamma}_i(t) \rangle_R \}, \tag{11}$$

where $\langle \tilde{\Gamma}_i(t) \tilde{\Gamma}_j(t') \rangle_R = \mathrm{Tr}_R[\tilde{R}_0 \tilde{\Gamma}_i(t) \tilde{\Gamma}_j(t')]$, $\tilde{\varrho}_I(t)$ is the reduced density operator of the atom in which a trace over the reservoir degrees of freedom has been performed, and $\tilde{R}_0$ is the reservoir part of the density operator. If we make the substitution $t' = t - \tau$ and assume the electromagnetic reservoir to be unoccupied, then Eq. (11) can be simplified to

$$[\dot{\tilde{\varrho}}_I]_1 = -\frac{1}{\hbar^2} \sum_{\substack{j=1,2,3 \\ i=4,5,6}} [\tilde{S}_i \tilde{S}_j \tilde{\varrho}_I(t) - \tilde{S}_j \tilde{\varrho}_I(t) \tilde{S}_i] \times \int_0^t d\tau \langle \tilde{\Gamma}_i(t) \tilde{\Gamma}_j(t-\tau) \rangle_R - \frac{1}{\hbar^2} \times \sum_{\substack{j=4,5,6 \\ i=1,2,3}} [\tilde{\varrho}_I(t) \tilde{S}_j \tilde{S}_i - \tilde{S}_i \tilde{\varrho}_I(t) \tilde{S}_j] \times \int_0^t d\tau \langle \tilde{\Gamma}_j(t-\tau) \tilde{\Gamma}_i(t) \rangle_R. \tag{12}$$

To facilitate the evaluation of the correlation integrals, we spectrally expand the time-dependent factors $f(t) \equiv c(t)s(t)$, $c^2(t)$, and $s^2(t)$ in $\tilde{\Gamma}_i$ as follows:

$$f(t) = \frac{1}{\sqrt{2\pi}} \int_{-\infty}^{\infty} f_\nu e^{i\nu t} d\nu \approx \frac{1}{\sqrt{2\pi}} \int_{-\nu_f/2}^{\nu_f/2} f_\nu e^{i\nu t} d\nu. \tag{13}$$

We assume above that the main spectral components of the functions $cs(t)$, $c^2(t)$, and $s^2(t)$ are around $\nu = 0$ with spectral widths ν_{cs}, ν_{c^2}, and ν_{s^2}, respectively. The details of the integral evaluation are provided in Appendix B. After some straightforward steps, we obtain the dressed state master equation in the Born-Markov approximation,

$$\dot{\tilde{\varrho}}_I = [\dot{\tilde{\varrho}}_I]_1 - \mathrm{Tr}_R[UB\dot{B}^\dagger U^\dagger(t), \tilde{\chi}_I(t)] \tag{14}$$

with

$$[\dot{\tilde{\varrho}}_I]_1 = -\frac{\gamma_0}{2} c^2 s^2 (\tilde{\varrho}_I - \tilde{R}_3 \tilde{\varrho}_I \tilde{R}_3) - \frac{\gamma_+}{2} c^4 (\tilde{R}_{22} \tilde{\varrho}_I - \tilde{R}_{12} \tilde{\varrho}_I \tilde{R}_{21}) - \frac{\gamma_-}{2} s^4 (\tilde{R}_{11} \tilde{\varrho}_I - \tilde{R}_{21} \tilde{\varrho}_I \tilde{R}_{12}) - \frac{cs}{2} e^{-2i\Omega t} [s^2 \gamma_0 (\tilde{R}_{12} \tilde{\varrho}_I - \tilde{R}_3 \tilde{\varrho}_I \tilde{R}_{12}) + c^2 \gamma_+ (\tilde{R}_{12} \tilde{\varrho}_I + \tilde{R}_{12} \tilde{\varrho}_I \tilde{R}_3) + s^2 \gamma_- (\tilde{\varrho}_I \tilde{R}_{12} - \tilde{R}_3 \tilde{\varrho}_I \tilde{R}_{12}) + c^2 \gamma_0 (\tilde{\varrho}_I \tilde{R}_{12} + \tilde{R}_{12} \tilde{\varrho}_I \tilde{R}_3)] - \frac{c^2 s^2}{2} e^{4i\Omega t} (\gamma_- + \gamma_+) \tilde{R}_{21} \tilde{\varrho}_I \tilde{R}_{21} + \mathrm{H.c.} \tag{15}$$

Here, γ_0 and γ_+ are the decay rates at the central and right Mollow bands defined in Appendix B, and the decay rate at the left Mollow side band is $\gamma_- = 2\pi \Sigma_\lambda |g_\lambda|^2 \delta[\omega_\lambda - \omega_L + 2\Omega(t)] \approx 2\pi \Sigma_\lambda |g_\lambda|^2 \delta[\omega_\lambda - \omega_L + 2\Omega(t) + \nu]$ for $\nu \in [-\nu_{s^2}/2, \nu_{s^2}/2]$. This corresponds to applying a local Markovian approximation around each of the Mollow frequencies ω_L and $\omega_L \pm 2\Omega(t)$.

The reduced density operator in the Schrödinger picture and bare atomic basis is given by $\varrho = B^\dagger U^\dagger \tilde{\varrho}_I UB$, so that its equation of motion reads

$$\dot{\varrho}(t) = \frac{d}{dt}(B^\dagger U^\dagger \tilde{\varrho}_I UB) = B^\dagger \dot{U}^\dagger \tilde{\varrho}_I UB + B^\dagger U^\dagger \tilde{\varrho}_I \dot{U}B + \dot{B}^\dagger U^\dagger \tilde{\varrho}_I UB + B^\dagger U^\dagger \tilde{\varrho}_I U\dot{B} + B^\dagger U^\dagger \dot{\tilde{\varrho}}_I UB. \tag{16}$$

Substituting Eq. (14) into Eq. (16) and using the facts that $\dot{U} = -\tilde{H}_0 U/i\hbar$, $\dot{U}^\dagger = \tilde{H}_0 U^\dagger / i\hbar$, and $\tilde{\varrho}_I = UB\varrho B^\dagger U^\dagger$, we obtain the radiative part of the master equation in the bare basis and Schrödinger picture,

$$\dot{\varrho}_{rad} = \frac{1}{i\hbar} B^\dagger \tilde{H}_0 U^\dagger (UB\varrho B^\dagger U^\dagger) UB - \frac{1}{i\hbar} B^\dagger U^\dagger (UB\varrho B^\dagger U^\dagger) U\tilde{H}_0 B + \dot{B}^\dagger U^\dagger (UB\varrho B^\dagger U^\dagger) UB + B^\dagger U^\dagger (UB\varrho B^\dagger U^\dagger) U\dot{B} + B^\dagger U^\dagger \{[\dot{\tilde{\varrho}}_I]_1 - [UB\dot{B}^\dagger U^\dagger(t), \tilde{\varrho}_I(t)]\} UB, \tag{17}$$

where $[\dot{\tilde{\varrho}}_I]_1$ is defined in Eq. (15). It follows that

$$\dot{\varrho}_{rad} = \frac{1}{i\hbar}[H_0, \varrho] + B^\dagger U^\dagger [\dot{\tilde{\varrho}}_I]_1 UB + \dot{B}^\dagger B\varrho + \varrho B^\dagger \dot{B} - \dot{B}^\dagger B\varrho + \varrho \dot{B}^\dagger B. \tag{18}$$

Using the fact that $\dot{B}^\dagger B = -B^\dagger \dot{B}$ (since B is a unitary operator), this simplifies to

$$\dot{\varrho}_{rad} = \frac{1}{i\hbar}[H_0, \varrho] + B^\dagger U^\dagger [\dot{\tilde{\varrho}}_I]_1 UB. \tag{19}$$

Using Eq. (15), we obtain finally

$$\dot{\varrho}_{rad} = -i\Omega R_3\varrho - \frac{\gamma_0}{2}c^2s^2(\varrho - R_3\varrho R_3) - \frac{\gamma_+}{2}c^4(R_{22}\varrho - R_{12}\varrho R_{21}) - \frac{\gamma_-}{2}s^4(R_{11}\varrho - R_{21}\varrho R_{12}) - \frac{cs}{2}[s^2\gamma_0(R_{12}\varrho - R_3\varrho R_{12}) + c^2\gamma_+(R_{12}\varrho + R_{12}\varrho R_3) + s^2\gamma_-(\varrho R_{12} - R_3\varrho R_{12}) + c^2\gamma_0(\varrho R_{12} + R_{12}\varrho R_3)] - \frac{c^2s^2}{2}(\gamma_- + \gamma_+)R_{21}\varrho R_{21} + \text{H.c.} \quad (20)$$

R_{ij} $(i,j=1,2)$ and R_3 are the dressed state atomic operators in Schrödinger picture and bare atomic basis,

$$R_{12} = cs\sigma_3 + c^2\sigma_{12} - s^2\sigma_{21},$$

$$R_{21} = cs\sigma_3 + c^2\sigma_{21} - s^2\sigma_{12},$$

$$R_3 = (c^2 - s^2)\sigma_3 - 2cs(\sigma_{12} + \sigma_{21}). \quad (21)$$

The dephasing of the quantum-dot dipole due to phonons is described by an additional contribution to the master equation [27],

$$\dot{\varrho}_{deph} = \frac{\gamma_p}{2}(c^2 - s^2)^2[R_3\varrho R_3 - R_3^2\varrho] + 2\gamma_p c^2s^2[R_{21}\varrho R_{12} - R_{12}R_{21}\varrho] + 2\gamma_p c^2s^2[R_{12}\varrho R_{21} - R_{21}R_{12}\varrho] + \text{H.c.}, \quad (22)$$

where γ_p represents the dipolar dephasing rate due to phonons.

Combining Eqs. (20) and (22), we arrive at the full master equation for the quantum-dot density operator in bare atomic basis,

$$\dot{\varrho} = -i\Omega R_3\varrho - \frac{\gamma_0c^2s^2 + \gamma_p(c^2 - s^2)^2}{2}(\varrho - R_3\varrho R_3) - \frac{\gamma_+c^4 + 4\gamma_pc^2s^2}{2}(R_{22}\varrho - R_{12}\varrho R_{21}) - \frac{\gamma_-s^4 + 4\gamma_pc^2s^2}{2}(R_{11}\varrho - R_{21}\varrho R_{12}) - \frac{cs}{2}[s^2\gamma_0(R_{12}\varrho - R_3\varrho R_{12}) + c^2\gamma_+(R_{12}\varrho + R_{12}\varrho R_3) + s^2\gamma_-(\varrho R_{12} - R_3\varrho R_{12}) + c^2\gamma_0(\varrho R_{12} + R_{12}\varrho R_3)] - \frac{c^2s^2}{2}(\gamma_- + \gamma_+)R_{21}\varrho R_{21} + \text{H.c.} \quad (23)$$

C. Jump model of the radiative decay rates

In the derivation of Eq. (23), we assumed that the local photonic density of states is smooth within the Mollow band regions $[\omega_L - \nu_{cs}/2, \omega_L + \nu_{cs}/2]$, $[\omega_L + 2\Omega - \nu_{c^2}/2, \omega_L + 2\Omega + \nu_{c^2}/2]$, and $[\omega_L - 2\Omega - \nu_{s^2}/2, \omega_L - 2\Omega + \nu_{s^2}/2]$ (local Markovian approximation) but presents a sharp jump at the band-edge frequency ω_E outside the above Mollow band regions (Fig. 2). Correspondingly, the smooth LDOS leads to the

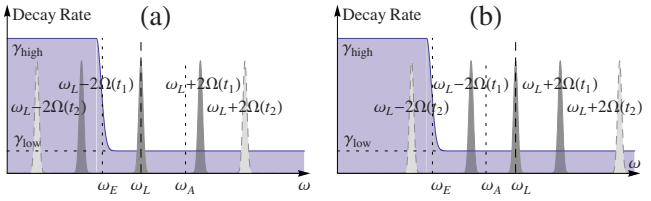

FIG. 3. (Color online) Decay rates for Mollow bands at different positions under the step-shaped LDOS model (see Fig. 2). The central Mollow band resides at ω_L and is time independent, with a fixed decay rate $\gamma_0 = \gamma_{low}$. The time-dependent right Mollow side band occurs at $\omega_L + 2\Omega(t)$, with possible positions at times t_1 [when $\epsilon(t_1)$ is small, shown as dark shaded peak] and t_2 [when $\epsilon(t_2)$ is large, shown as light shaded peak] shown schematically. In general, the right-side band experiences a fixed decay rate $\gamma_+ = \gamma_{low}$. The decay rate at the left Mollow side band $\omega_L - 2\Omega(t)$, however, depends on the relative magnitudes of Mollow splitting $2\Omega(t)$ and Δ_{LE}. Two parameter configurations are considered: (a) $\Delta_{AL} > 0$ and with $|\Delta_{AL}| > \Delta_{LE}$. Here, the left side band resides at the high LDOS region with a fixed decay rate $\gamma_- = \gamma_{high}$ since $2\Omega(t) > \Delta_{LE}$. (b) $\Delta_{AL} < 0$ and with $|\Delta_{AL}| < \Delta_{LE}$. Here the left side band is in the low LDOS region with $\gamma_- = \gamma_{low}$ when $\epsilon(t_1)$ is small (dark shaded peak) but is in the high LDOS region with $\gamma_- = \gamma_{high}$ when $\epsilon(t_2)$ is large (light shaded peak).

radiative decay rates γ_0, γ_+, and γ_- at the central, right, and left Mollow bands. The values of those decay rates are dependent on whether their corresponding Mollow bands fall within the high LDOS region or the low LDOS region. In our model (see Fig. 3), the central and right Mollow bands are always in the low LDOS region with a decay rate γ_{low}. So we always have $\gamma_0 = \gamma_+ = \gamma_{low}$. The left Mollow side band, however, can be in either the low LDOS region or the high LDOS region, depending on the relative size of the Mollow splitting $2\Omega(t)$ and the field-band-edge detuning $\Delta_{LE} = \omega_L - \omega_E$. When $2\Omega(t) < \Delta_{LE}$, the left Mollow side band is in the low LDOS region, with $\gamma_- = \gamma_{low}$. On the other hand, when $2\Omega(t) > \Delta_{LE}$, the left Mollow side band is in the high LDOS region, with $\gamma_- = \gamma_{high}$. We consider two parameter configurations as follows:

(i) $\Delta_{AL} > 0$ and with $\Delta_{AL} > \Delta_{LE}$ [Fig. 3(a)]. In this configuration, we always have $2\Omega(t) \geq \Delta_{AL} > \Delta_{LE}$, so that the left Mollow side band experiences a constant radiative decay rate $\gamma_- = \gamma_{high}$.

(ii) $\Delta_{AL} < 0$ and with $|\Delta_{AL}| < \Delta_{LE}$ [Fig. 3(b)]. In this configuration, as the Rabi frequency $\epsilon(t)$ changes between 0 and the peak Rabi frequency ϵ_p, the left Mollow side band can move from the low LDOS region to the high LDOS region or vice versa. As a result, $\gamma_- = \gamma_{low}$ in the low LDOS region but changes to $\gamma_- = \gamma_{high}$ when moved to the high LDOS region. Note that at the immediate vicinity of the band-edge frequency ω_E where LDOS jump occurs (Fig. 3), our local Markovian approximation does not apply and γ_- does not have a well defined value. Since this happens only during a very short time scale compared with the entire pulse, we assume this has a negligible effect on the overall time evolution of the system.

The step LDOS model assumption is only an approximation to the LDOS peak provided by the waveguide mode cutoff. In reality, the LDOS peak has a finite spectral width

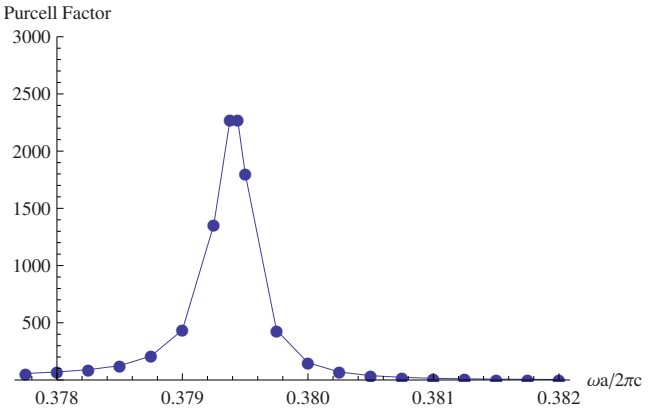

FIG. 4. (Color online) Purcell factor near a photonic band edge formed by waveguide inside a 3D-2D photonic crystal heterostructure. Details of the structure are given in Ref. [9].

ν_{LDOS} instead of an infinitely wide plateau. The realizable value of γ_{high} is also limited in reality by random disorder within the waveguide and finite length of the waveguide segment. The achievable LDOS around a photonic band edge in realistic structures has been studied before using finite difference time domain simulations [9]. A 3D-2D photonic crystal heterostructure with inverse square spiral structures as the 3D cladding layers and square lattice structure as 2D PC slabs was used during the simulation. Although the result shown in [9] is the simulated LDOS in arbitrary units, actual Purcell factors are readily determined from the simulation program. We present in Fig. 4 a recalculation of unpublished results for the Purcell factors around a photonic band edge formed by a waveguide cutoff in a 3D-2D PBG heterostructure (details of structure given in Ref. [9]). Purcell factors up to 2300 are achievable for a 15 unit cell length (9 μm for light with vacuum wavelength $\lambda \approx 1.5$ μm) waveguide in this example as shown in Fig. 4. If we assume the atomic decay rates in ordinary vacuum to be on the order of GHz, then the peak Purcell factor of 2300 would correspond to a decay rate around 2.3 THz and a subpicosecond decay time. Furthermore, the full width half maximum (FWHM) of the band-edge Purcell factor peak is $\nu_{\mathrm{LDOS}} \approx 0.0006 \frac{2\pi c}{a}$, where a is the lattice constant of the 2D microchip layer of the 3D-2D heterostructure. For a typical 1.5 μm wavelength in photonics applications, $a \approx 600$ nm is required [9], so that $\nu_{\mathrm{LDOS}} \approx 1.88$ THz. In order to apply our step LDOS model, the shape and duration of the envelop function $\mathcal{E}(t)$ must be such that the spectral widths ν_{s^2} of the dressed state coefficient function associated with the left Mollow side band are much smaller than ν_{LDOS}. If we approximate ν_{s^2} with the pulse spectral width ν_L, then the condition $\nu_L < \nu_{\mathrm{LDOS}}$ corresponds to a picosecond minimum duration for smooth pulses.

III. ATOMIC BLOCH VECTOR EQUATION FOR COLORED VACUUM

In this section we derive equation governing the time evolution of atomic population and polarization in our "structured electromagnetic vacuum." This emerges from taking the expectation values of the atomic operators with respect to the atomic density operator. The density operator satisfies a Heisenberg equation of motion (the master equation) described in Sec. II. We demonstrate the occurrence of certain vacuum structure terms in the Bloch equation that significantly alters the time evolution of the atomic Bloch vector as the atom interacts with an optical pulse. In addition, we demonstrate the occurrence of strongly field-dependent relaxation rates for the atomic Bloch vector components that enable near-complete inversion of the atomic population as the optical pulse subsides. Both of these features are absent in a conventional (unstructured) electromagnetic vacuum. We define the following atomic dipole operators:

$$\sigma_1 = \sigma_{12} + \sigma_{21},$$

$$\sigma_2 = i(\sigma_{12} - \sigma_{21}). \tag{24}$$

σ_1 and σ_2 represent the in-phase and in-quadrature parts of the dipole moment, respectively. Using Eq. (23) and setting $\gamma_0 = \gamma_+$ for our LDOS model, the following Bloch component equations are obtained (details given in Appendix C):

$$\langle \dot{\sigma}_1 \rangle = -\Delta_{AL}\langle \sigma_2 \rangle - \frac{1}{T_u}\langle \sigma_1 \rangle + V,$$

$$\langle \dot{\sigma}_2 \rangle = \Delta_{AL}\langle \sigma_1 \rangle + 2\epsilon\langle \sigma_3 \rangle - \frac{1}{T_v}\langle \sigma_2 \rangle,$$

$$\langle \dot{\sigma}_3 \rangle = -2\epsilon\langle \sigma_2 \rangle - \frac{1}{T_w}(\langle \sigma_3 \rangle + 1) + V\langle \sigma_1 \rangle. \tag{25}$$

Here, $1/T_{u,v} = [c^2(1+s^2)\gamma_+ + s^4\gamma_- + 4\gamma_p]/2 \mp c^2 s^2(\gamma_+ - \gamma_-)/2$, $1/T_w = c^2(1+s^2)\gamma_+ + s^4\gamma_-$, and $V = (\gamma_+ - \gamma_-)cs^3$. T_u and T_v reduce to the transverse dephasing time and T_w reduces to the longitudinal dephasing time in ordinary vacuum if we set $\gamma_+ = \gamma_-$. V is a novel vacuum structure term arising purely from the jump structure of the electromagnetic vacuum.

The Bloch component equations can be written in vector form,

$$\dot{\boldsymbol{\rho}} = \boldsymbol{\Omega} \times \boldsymbol{\rho} - \boldsymbol{\Gamma}_{\boldsymbol{\rho}} + \mathbf{C}, \tag{26}$$

where

$$\boldsymbol{\rho} = (\langle \sigma_1 \rangle, \langle \sigma_2 \rangle, \langle \sigma_3 \rangle) = (u, v, w), \quad \boldsymbol{\Omega} = (-2\epsilon, 0, \Delta_{AL}),$$

$$\boldsymbol{\Gamma}_{\boldsymbol{\rho}} = (u/T_u, v/T_v, w/T_w), \quad \mathbf{C} = (V, 0, -1/T_w + Vu).$$

The atomic Bloch vector $\boldsymbol{\rho}$ describes a "mixed state" and is free to evolve anywhere inside the unit sphere $u^2 + v^2 + w^2 \leq 1$. The effects of the structured vacuum appear through $\boldsymbol{\Gamma}_{\boldsymbol{\rho}}$ and $\mathbf{C}$. Unlike the constant longitudinal and transverse relaxation times in ordinary vacuum, the atom experiences field-dependent longitudinal and transverse relaxation times T_u, T_v, and T_w due to the density of state jump. The combined effect of these field-dependent relaxation rates and the vacuum structure term is a dynamical evolution of the Bloch vector dramatically different from that in ordinary vacuum. Under suitable steady-state pumping conditions, the single-atom population inversion w is known to exhibit a weak switching effect [27] at a certain threshold Rabi fre-

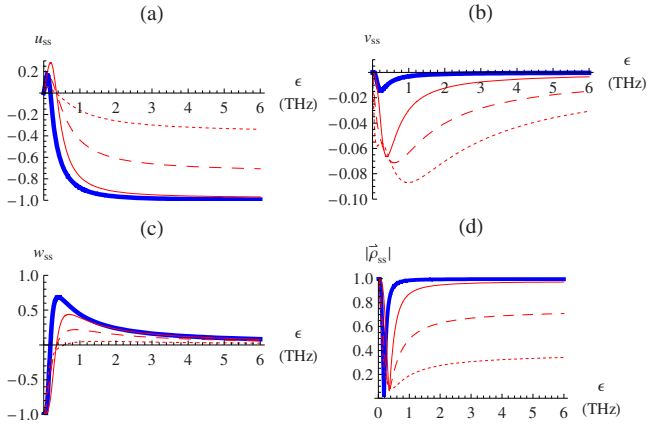

FIG. 5. (Color online) The steady-state value of (a) u_{ss}, (b) v_{ss}, (c) w_{ss}, and (d) the norm of the Bloch vector $|\boldsymbol{\rho}_{ss}|$ as functions of the laser beam Rabi frequency ϵ_0 for different photonic decay rate contrast ratios γ_-/γ_+ and phonon dephasing rates γ_p. $\Delta_{AL}=1$ THz, $\gamma_-=2.5$ THz, and $\gamma_-/\gamma_+=1000$, $\gamma_p=0$ THz (thick solid lines); $\gamma_-/\gamma_+=100$, $\gamma_p=0$ THz (solid lines); $\gamma_-/\gamma_+=100$, $\gamma_p=0.1$ THz (dashed lines); and $\gamma_-/\gamma_+=100$, $\gamma_p=0.5$ THz (dotted lines).

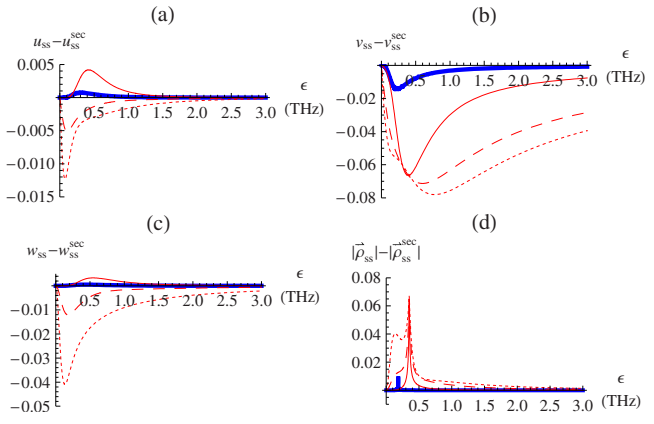

FIG. 6. (Color online) Comparison of the steady-state solution [Eq. (27)] with Eq. (28): (a) $u_{ss}-u_{ss}^{sec}$, (b) $v_{ss}-v_{ss}^{sec}$, (c) $w_{ss}-w_{ss}^{sec}$, and (d) $|\boldsymbol{\rho}_{ss}|-|\boldsymbol{\rho}_{ss}^{sec}|$ as functions of the laser beam Rabi frequency ϵ_0 for different photonic decay rate contrast ratios γ_-/γ_+ and phonon dephasing rates γ_p. $\Delta_{AL}=1$ THz, $\gamma_-=2.5$ THz, and $\gamma_-/\gamma_+=1000$, $\gamma_p=0$ THz (thick solid lines); $\gamma_-/\gamma_+=100$, $\gamma_p=0$ THz (solid lines); $\gamma_-/\gamma_+=100$, $\gamma_p=0.1$ THz (dashed lines); and $\gamma_-/\gamma_+=100$, $\gamma_p=0.2$ THz (dotted lines).

quency. This steady-state switching effect has been studied previously in the linear response framework [27]. Our Bloch vector equation describes the complete nonlinear response of the atom to both steady-state control field and strong signal pulses. Moreover our complete nonlinear and dynamical treatment of the response of the atom to strong control pulses reveals a much larger and more robust optical switching and inversion than is evident from linearized or steady-state descriptions.

IV. STEADY-STATE SWITCHING AND FIELD DEPENDENT RELAXATION

To provide background for the dynamical switching phenomena presented in Sec. V and as a diagnostic of our generalized Bloch vector equation, we first discuss the steady-state properties of Eq. (26) with a constant driving beam.

If $\epsilon(t)=\epsilon_0$ is a constant (cw laser), then by setting $\dot{\boldsymbol{\rho}}=0$, we obtain the steady-state solution of Eq. (26),

$$Du_{ss} = 2\epsilon_0\Delta_{AL}T_uT_v + V(T_u + 4\epsilon_0^2T_uT_vT_w),$$

$$Dv_{ss} = -2\epsilon_0T_v + VT_uT_v(\Delta_{AL} + 2\epsilon_0VT_w),$$

$$Dw_{ss} = -1 - \Delta_{AL}^2T_uT_v + VT_uT_w(V - 2\epsilon_0\Delta_{AL}T_v), \quad (27)$$

where $D\equiv 1+4\epsilon_0^2T_vT_w+\Delta_{AL}^2T_uT_v+2\epsilon_0V\Delta_{AL}T_uT_vT_w$. If we assume $\Delta_{AL}>\Delta_{LE}>0$, so that $\gamma_-\equiv\gamma_{high}$ and $\gamma_+\equiv\gamma_{low}$, then as shown in Fig. 5, the steady-state solution [Eq. (27)] exhibits switching of the population w_{ss} and in-phase part of the dipole moment u_{ss} at certain threshold values ϵ_{thr}. This threshold depends on the ratio γ_-/γ_+ of the decay rates at the left and right Mollow side bands, as well as the phonon dephasing rate γ_p. The in-quadrature part of the dipole moment v_{ss} is usually very small, especially for high γ_-/γ_+ ratios, low γ_p, and strong fields. The norm of the Bloch vector exhibits a dip around ϵ_{thr}, but it can be shown algebraically from Eq. (27) that $\lim_{\epsilon_0/\Delta_{AL}\to\infty}|\boldsymbol{\rho}_{ss}|=(\gamma_--\gamma_+)/(\gamma_-+\gamma_++8\gamma_p)$. For small γ_p and γ_+ compared with γ_-, this strong-field limit of Bloch vector norm is very close to 1. The switching effect does not exist for $\Delta_{AL}<0$, $\gamma_-=\gamma_{high}$, and $\gamma_+=\gamma_{low}$. However, we will not consider that parameter region for now.

A simplified algebraic expression of the steady-state dipole moments and population inversion has been derived previously [27] by ignoring some of the "nonsecular" terms during the derivation of the master equation [Eq. (23)]. With some simple change of notations, this simplified steady state [27] can be expressed as

$$w_{ss}^{sec} = (c^2 - s^2)R_3^{sec},$$

$$u_{ss}^{sec} = -2csR_3^{sec},$$

$$v_{ss}^{sec} = 0, \quad (28)$$

with $R_3^{sec}=(s^4\gamma_--c^4\gamma_+)/(s^4\gamma_-+c^4\gamma_++8c^2s^2\gamma_p)$. Figure 6 shows the difference between Eqs. (27) and (28). It can be seen that for low temperature (small γ_p), Eq. (28) is a good approximation of Eq. (27) except near the switching threshold. The differences between the two solutions become more significant for smaller contrast ratios γ_-/γ_+ and higher temperatures (larger γ_p).

A noteworthy feature of the steady-state solution [Eq. (27)] is that except for the neighborhood of the switching threshold, the steady-state Bloch vector $\boldsymbol{\rho}_{ss}$ always aligns closely with the torque vector $\boldsymbol{\Omega}$. In other words, $\theta\approx 0$ or $\theta\approx\pi$ with θ being the angle between $\boldsymbol{\rho}_{ss}$ and $\boldsymbol{\Omega}$. This can be seen by looking at the steady-state equation for the in-quadrature component of the Bloch vector, $0=\dot{v}_{ss}=\Delta_{AL}u_{ss}-v_{ss}/T_v+2\epsilon w_{ss}$. This can be solved approximately by observing that v_{ss} remains very small throughout the evolution [Fig. 5(b)]. Using $v_{ss}\approx 0$, we obtain

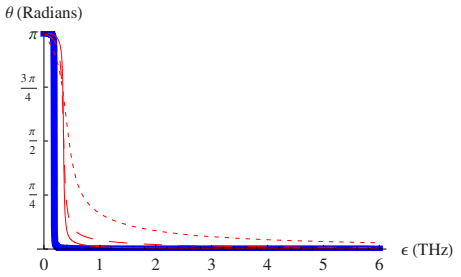

FIG. 7. (Color online) Relative angle θ between the steady-state atomic Bloch vector $\boldsymbol{\rho}_{ss}$ and the laser beam torque vector $\boldsymbol{\Omega}$, as a function of the laser beam Rabi frequency ϵ_0, for different photonic decay rate contrast ratios γ_-/γ_+ and phonon dephasing rates γ_p. $\Delta_{AL}=1$ THz, $\gamma_-=2.5$ THz, and $\gamma_-/\gamma_+=1000$, $\gamma_p=0$ THz (thick solid lines); $\gamma_-/\gamma_+=100$, $\gamma_p=0$ THz (solid lines); $\gamma_-/\gamma_+=100$, $\gamma_p=0.1$ THz (dashed lines); and $\gamma_-/\gamma_+=100$, $\gamma_p=0.5$ THz (dotted lines).

$$\rho_{ss}^x/\rho_{ss}^y \equiv u_{ss}/w_{ss} \approx -2\epsilon/\Delta_{AL} \equiv \Omega_x/\Omega_y. \tag{29}$$

This implies that $\boldsymbol{\rho}_{ss}$ and $\boldsymbol{\Omega}$ remain nearly parallel. In the limit of $\gamma_+ \to \infty$ (in which case there is no clearly defined threshold) any nonzero value of ϵ_0 will bring the system to positive population inversion. Regardless of the value of ϵ_0, $\boldsymbol{\rho}_{ss}$ always aligns parallel to $\boldsymbol{\Omega}$ ($\theta=0$). When γ_+ is finite, perfect alignment of $\boldsymbol{\rho}_{ss}$ with $\boldsymbol{\Omega}$ is not always achieved. However, except near the switching threshold, $\theta \approx 0$ or $\theta \approx \pi$ still remains true, especially for high γ_-/γ_+ ratios and small γ_p, as shown in Fig. 7. The alignment of $\boldsymbol{\rho}_{ss}$ with $\boldsymbol{\Omega}$ is most evident for large ϵ_0. For $\Delta_{AL}>0$ and no inversion when $\epsilon_0 < \epsilon_{thr}(w_{ss}<0)$, u_{ss} is positive and $\boldsymbol{\rho}_{ss}^{inst}$ is nearly antiparallel to the torque vector $\boldsymbol{\Omega}=(-2\epsilon,0,\Delta_{AL})$ ($\theta=\pi$). In the structured electromagnetic vacuum, w_{ss} becomes positive after inversion when $\epsilon_0 > \epsilon_{thr}$ and the corresponding sign change in u_{ss} describes switching of the steady-state Bloch vector $\boldsymbol{\rho}_{ss}$ from antiparallel to parallel alignment with $\boldsymbol{\Omega}$ ($\theta=0$). As shown in Sec. V, the realignment of $\boldsymbol{\rho}_{ss}$ with $\boldsymbol{\Omega}$ provides a precondition for achieving dynamical inversion that is much higher than the steady-state inversion w_{ss}.

We now study the rate at which the atom relaxes to its steady state. The decay rates $1/T_u$, $1/T_v$, and $1/T_w$ in the Bloch equation [Eq. (26)] are field dependent, as shown in Fig. 8. Both $1/T_u$ and $1/T_w$ increase monotonically with ϵ_0.

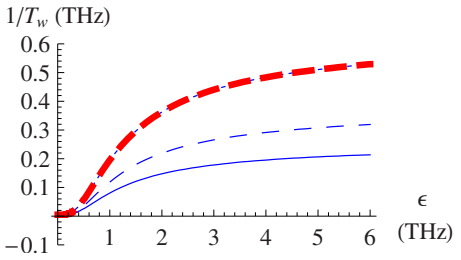

FIG. 8. (Color online) Decay rate of the population inversion for different γ_-/γ_+ ratios and γ_p. $\Delta_{AL}=1$ THz, $\gamma_+=5$ GHz, and $\gamma_-=1$ THz, $\gamma_p=0$ THz (solid lines); $\gamma_-=1.5$ THz, $\gamma_p=0$ THz (dashed lines); $\gamma_-=2.5$ THz, $\gamma_p=0$ THz (dotted lines); and $\gamma_-=2.5$ THz, $\gamma_p=0.5$ THz (thick dashed lines).

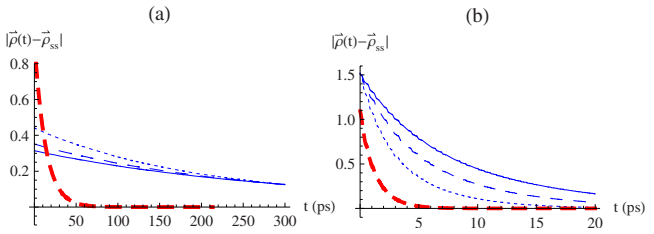

FIG. 9. (Color online) Relaxation of $\boldsymbol{\rho}(t)$ toward $\boldsymbol{\rho}_{ss}$ for different γ_-/γ_+ ratios and γ_p. (a) $\epsilon_0=0.3$ THz, around the threshold values; (b) $\epsilon_0=6$ THz, far above threshold values. $\Delta_{AL}=1$ THz, $\gamma_+=5$ GHz, and $\gamma_-=1$ THz, $\gamma_p=0$ THz (solid lines); $\gamma_-=1.5$ THz, $\gamma_p=0$ THz (dashed lines); $\gamma_-=2.5$ THz, $\gamma_p=0$ THz (dotted lines); and $\gamma_-=2.5$ THz, $\gamma_p=0.5$ THz (thick dashed lines).

Unlike in ordinary vacuum, $1/T_u \neq 1/T_v$ in general due to the asymmetry between γ_+ and γ_-. γ_p has a strong effect on the dipole dephasing rates $1/T_u$ and $1/T_v$, but it does not affect $1/T_w$ significantly. The combined effect of $1/T_u$, $1/T_v$, and $1/T_w$ is a field-dependent effective decay rate $1/T_{\boldsymbol{\rho}}$ of the Bloch vector $\boldsymbol{\rho}(t)$ toward its steady-state value $\boldsymbol{\rho}_{ss}$. A simple analytic expression of $1/T_{\boldsymbol{\rho}}$ is not available. Instead, we perform numerical simulations of the relaxation process of $\boldsymbol{\rho}$ toward $\boldsymbol{\rho}_{ss}$, shown as the decay of the distance $|\boldsymbol{\rho}-\boldsymbol{\rho}_{ss}|$ between $\boldsymbol{\rho}$ and $\boldsymbol{\rho}_{ss}$. As shown in Fig. 8, the population relaxation rates in general increase with ϵ_0. Figure 9 shows the relaxation of $|\boldsymbol{\rho}-\boldsymbol{\rho}_{ss}|$ for a small Rabi frequency around the switching threshold [Fig. 9(a)] and for a high Rabi frequency [Fig. 9(b)] far above the threshold. The relaxation of the Bloch vector is much slower for Rabi frequency near the switching threshold (on the order of 10^2 ps) than far above the threshold (on the order of several ps). As a result of this slow relaxation for weak fields, it is not practical to utilize this steady-state effect for ultrafast switching even though w_{ss} presents switching with respect to ϵ_0. An ultrafast steady-state switching device using collective atomic response has been proposed [27,33]. However, we will focus on single-atom or independent atoms in this paper. Strong field relaxation of the Bloch vector toward steady state is much faster. This would allow ultrafast steady-state switching at the cost of a much smaller population inversion [Fig. 5(c)] and a much higher power consumption. It is therefore important to go beyond the steady-state picture to achieve switching with high speed, high-contrast ratio, and low power consumption simultaneously.

V. DYNAMIC SWITCHING AND NEAR COMPLETE INVERSION

The field-dependent relaxation rates provide an unprecedented opportunity to dynamically control the time regimes of strong-coupling dynamics in real time. For example, if a single smooth pulse with proper time duration is strong enough, then the Purcell enhanced radiative decay rates due to increased coupling to the band edge near the peak of the pulse would surpass the transient oscillations and attract the system into the steady-state regime (III) (Fig. 1). On the other hand, during the weak field of the pulse precursor and tail, the radiative decay rates fall significantly below the co-

herent transient evolution rate due to decreased coupling from the band edge, so that the system escapes from the steady state and enters the coherent transient regime (I) (Fig. 1). The time-averaged radiative decay rates would be on the same order of magnitude as the pulse duration, so that overall the system belongs to time regime (II) in Fig. 1. However, on closer examination, as the electromagnetic field strength rises and falls with the pulse, the system essentially alternates between the steady-state regime (III) and the transient regime (I). As discussed in Sec. IV, the new vacuum structure term in the Bloch equation enables unusual steady-state switching effects unattainable in a smooth LDOS environment. By combining this steady-state switching with coherent dynamics, novel nonlinear Bloch vector dynamics, unique to a structured vacuum, is uncovered.

In this section, we illustrate an unusual dynamic quantum-dot population switching mechanism due to the interplay between steady-state attraction and coherent dynamics. If the driving laser field satisfies the steady-state attraction condition and adiabatic following condition (to be discussed in Sec. V A), the transient dynamics of adiabatic following as the pulse subsides brings the system to either near-complete inversion or the ground state. Unlike the steady-state switching, nonlinear dynamics in the colored vacuum offers high switching speed, high switching contrast, and low power consumption simultaneously.

A. Quasisteady adiabatic pulse

In order to realize the chorus between different time regimes during the dynamic switching proposed above and achieve maximum population switching contrast, certain conditions should be satisfied by the exciting optical pulse.

We define an adiabatic pulse as one whose torque vector speed (roughly characterized by the rate of change of the Rabi frequency scaled by detuning $|\Delta_{AL}|$) is much smaller than the precession frequency $|\mathbf{\Omega}|$ of the Bloch vector around the torque vector $\mathbf{\Omega}$,

$$\frac{d\epsilon(t)}{dt}\frac{1}{|\Delta_{AL}|} \ll |\mathbf{\Omega}|. \tag{30}$$

The conditions for a quasisteady pulse in a colored vacuum, however, are more complex than in free space. In ordinary vacuum, the steady-state Bloch vector varies smoothly with the pulse Rabi frequency and the relaxation rates are field independent. Consequently, we can loosely define a quasisteady pulse as one that satisfies $\dot{\epsilon}(t)/|\Delta_{AL}| \ll 1/T_{\boldsymbol{\rho}}$. In this case, the decay rate of the Bloch vector toward the instantaneous steady state is much faster than the rate of change of the instantaneous steady state. As a result, the evolution of the Bloch vector closely follows that of the instantaneous steady state caused by the change of the Rabi frequency $\epsilon(t)$. In the colored vacuum described in Sec. IV, the instantaneous steady state changes dramatically near the switching threshold, and $1/T_{\boldsymbol{\rho}}$ is strongly field dependent. To capture those unusual features, we give a more precise definition of quasisteady pulses. In the absence of a simple analytic expression of $1/T_{\boldsymbol{\rho}}$, we use $|\mathbf{\Gamma}|=|(1/T_u, 1/T_v, 1/T_w)|$ as a simplified approximant for $1/T_{\boldsymbol{\rho}}$. We define a pulse as quasisteady if for a large enough time duration τ_{qs} (called the steady-state attraction interval) around the peak, t_p, of the pulse envelop function, the following steady-state attraction conditions hold:

$$\left|\frac{d\boldsymbol{\rho}_{ss}^{inst}(\epsilon(t))}{dt}\right| \ll |\mathbf{\Gamma}| \quad \text{for } t \in \left[t_p - \frac{\tau_{qs}}{2}, t_p + \frac{\tau_{qs}}{2}\right], \tag{31a}$$

$$\frac{1}{\tau_{qs}} \ll |\mathbf{\Gamma}|. \tag{31b}$$

Here, $\boldsymbol{\rho}_{ss}^{inst}(\epsilon(t))$ is the instantaneous steady state at time t defined as $\boldsymbol{\rho}_{ss}(\epsilon_0=\epsilon(t))$ in Eq. (27). Condition Eq. (31a) means the change rate of the instantaneous steady state caused by the temporal variation of the pulse envelop is much smaller than the relaxation rate of the Bloch vector. This enables the Bloch vector to closely follow the instantaneous steady state near the peak of the pulse. Unlike in an unstructured electromagnetic vacuum, the relaxation rates are strongly field dependent. While $|\mathbf{\Gamma}|$ can be large (in the order of THz) for the strong field near the peak of the pulse, it becomes much smaller near the leading and trailing edges of the pulse. Indeed, for pulses of interest to us, the quantum-dot switching threshold occurs considerably below the peak of the pulse where the instantaneous steady state changes dramatically. The condition [Eq. (31a)] does not hold throughout the duration of such a pulse. However, we only require that Eq. (31a) holds for a sufficiently long time duration, τ_{qs}, near the peak of the pulse. This enables the Bloch vector to relax to the instantaneous steady state $\boldsymbol{\rho}_{ss}^{inst}(\epsilon_p)$ of the peak Rabi frequency, ϵ_p, far above the switching threshold, ϵ_{thr}. This "steady-state attraction" requires the approximate relaxation time to be short compared to τ_{qs}, a condition that is expressed in Eq. (31b).

For concreteness, we consider a Gaussian pulse with temporal Rabi frequency profile,

$$\epsilon(t) = \epsilon_p e^{-[(t-t_p)/\tau]^2}. \tag{32}$$

Here, τ is the pulse duration, t_p is pulse peak time, and ϵ_p is the peak Rabi frequency. Figure 10 illustrates condition [Eq. (31)] applied to a Gaussian pulse with FWHM of 15 ps, $\epsilon_p=6$ THz, and $t_p=30$ ps. The decay rates are $\gamma_-=2.5$ THz, $\gamma_+=5$ GHz, $\gamma_p=0$ and the detuning $\Delta_{AL}=2$ THz. The shaded area shows the scaled temporal profile of $\epsilon(t)$. The darker the shade, the better the condition [Eq. (31a)] is satisfied, with $|d\boldsymbol{\rho}_{ss}^{inst}(\epsilon(t))/dt|$ (solid curve) much smaller than $|\mathbf{\Gamma}|$ (dashed curve). Clearly the leading and trailing edges of the pulse do not satisfy the steady-state attraction condition. However, for a duration $\tau_{qs}\approx 20$ ps around t_p, steady-state attraction does occur. This is sufficient for this pulse to be categorized as quasisteady. A pulse is "quasisteady adiabatic" if both Eqs. (31) and (30) hold simultaneously. It is easy to verify that the Gaussian pulse shown in Fig. 10 is in fact a quasisteady adiabatic pulse.

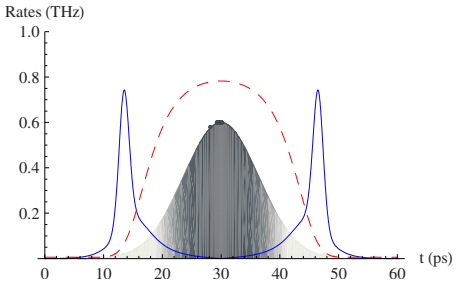

FIG. 10. (Color online) The steady-state attraction condition [Eq. (31)] applied to a Gaussian pulse with $\tau=15$ ps, $\epsilon_p=6$ THz, and $t_p=30$ ps. The solid curve is $|d\boldsymbol{\rho}_{ss}^{inst}(\epsilon(t))/dt|$ and the dashed curve is $|\boldsymbol{\Gamma}|$. The shaded area shows the scaled temporal profile of the pulse Rabi frequency, with the darkness of the shading representing the degree to which condition [Eq. (31)] is satisfied. All rates are in THz.

B. Dynamic quantum-dot inversion via steady-state attraction and adiabatic following

When both the steady-state attraction condition [Eq. (31)] and adiabatic following condition [Eq. (30)] are satisfied, the evolution of the strongly coupled quantum-dot system can be described as a steady-state attraction near the pulse peak followed by a coherent adiabatic following process when the pulse subsides. When $\Delta_{AL}>0$, the combination of these two processes leads to a dynamic inversion mechanism belonging to time regime (II) in Fig. 1.

Figure 11(a) depicts the 3D Bloch vector evolution path

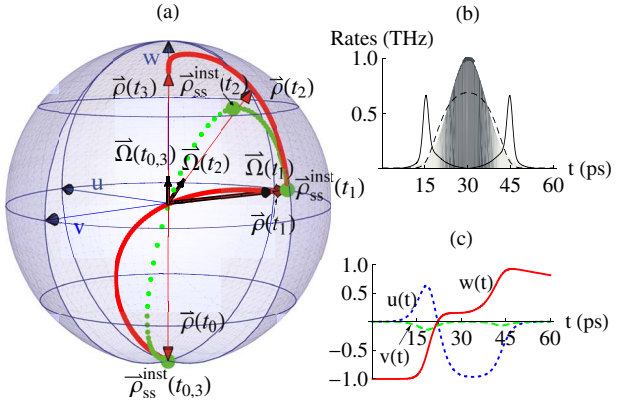

FIG. 11. (Color online) Dynamical inversion of a two-level atom. $\gamma_-=2.5$ THz, $\gamma_+=5$ GHz, $\gamma_p=0$ THz, $\Delta_{LE}=1$ THz, $\Delta_{AL}=2$ THz, $\epsilon_p=6$ THz, $t_0=0$ ps, $t_1=32.5$ ps, $t_2=42.5$, $t_3=60$ ps, and $\tau=15$ ps. (a) 3D evolution path of the Bloch vector $\boldsymbol{\rho}(t)$ (red solid curve). The (red) thin vectors are Bloch vectors at different times, while the (black) thick vectors are the corresponding torque vectors. The big (green) dots are the instantaneous steady states at different times, while the dotted (green) curve shows the evolution path of the instantaneous steady states. (b) Scaled temporal profile of the pulse Rabi frequency, with the darkness of the shading representing how well condition [Eq. (30)] is satisfied. The solid curve is $|d\boldsymbol{\rho}_{ss}^{inst}(\epsilon(t))/dt|$ and the dashed curve is $|\boldsymbol{\Gamma}|$; all rates are in THz. (c) 2D plot of the dipole moments $u(t)$ (blue dotted curve), $v(t)$ (green dashed curve), and population inversion $w(t)$ (red solid curve) as functions of time.

exhibiting dynamical inversion by the Gaussian pulse shown in Fig. 10, with $\gamma_-=\gamma_{high}$, $\gamma_+=\gamma_{low}$, and $\Delta_{AL}>0$. Figure 11(c) shows the corresponding 2D plots of $u(t)$, $v(t)$, and $w(t)$ as functions of time. The evolution process can be divided into the following two distinct stages:

(i) *Steady-state attraction process* (*time regime III of Fig. 1*). In this stage, the atom starts from the ground state $\boldsymbol{\rho}(t_0=0)$. As the optical pulse impinges on the atomic dipole, it begins to Mollow split the atomic energy levels (in the instantaneous steady-state picture), with the left side band appearing in the high LDOS region (with an effective decay rate $\gamma_-=2.5$ THz), while the center and right side bands remain in the low LDOS region (with an effective decay rate $\gamma_+=5$ GHz). The vacuum structure appears in the atomic Bloch equation [Eq. (26)] as an asymmetry in the Mollow side band decay rates $\gamma_\pm$. The result is a highly field-dependent instantaneous steady state $\boldsymbol{\rho}_{ss}^{inst}$ [its evolution path shown as the (green) dotted curve in Fig. 11(a)], which switches from antiparallel to parallel alignment with the pulse torque vector (thick black vectors) as the pulse strength surpasses the steady-state threshold. $\boldsymbol{\rho}_{ss}^{inst}$ approaches the (green) steady-state spot $\boldsymbol{\rho}_{ss}^{inst}(t_1)$ in Fig. 11(a) as the peak of the pulse arrives, where $\boldsymbol{\rho}_{ss}^{inst}(t_1)$ represents the inverted instantaneous steady state at time $t_1=32.5$ ps around the peak of the pulse $t_p=30$ ps, with $\boldsymbol{\rho}_{ss}^{inst}[\epsilon(t_1)]\approx\boldsymbol{\rho}_{ss}^{inst}(\epsilon_p)$. Since the pulse satisfies the steady-state attraction condition [Eq. (31)] around the peak, the rapid relaxation rates of the actual Bloch vector toward its instantaneous steady state quickly pull $\boldsymbol{\rho}$ (thin red vectors) toward $\boldsymbol{\rho}_{ss}^{inst}(t_1)$. This steady-state attraction process is much faster than adiabatically (steadily) inverting the atom with a slowly varying weak field that passes over the switching threshold. By time t_1, $\boldsymbol{\rho}(t_1)$ has almost reached $\boldsymbol{\rho}_{ss}^{inst}(t_1)$ and is well aligned (parallel) with the torque vector $\boldsymbol{\Omega}(t_1)$ of the driving laser field.

(ii) *Adiabatic following process* (*time regime I of Fig. 1*). In this second stage, the pulse has passed its peak and is declining in strength. In order to more clearly separate and elucidate the different stages, we consider an extended pulse. The final outcome of high inversion is also achieved with much shorter pulses. The second stage is the adiabatic following process from t_1 to $t_3=60$ ps. The torque vector evolves from $\boldsymbol{\Omega}(t_1)$ to $\boldsymbol{\Omega}(t_3)$. Since our illustrative pulse satisfies the adiabatic following condition [Eq. (30)], the Bloch vector $\boldsymbol{\rho}$ adiabatically follows the change of the torque vector from $\boldsymbol{\rho}(t_1)$ to $\boldsymbol{\rho}(t_3)$, approaching a highly inverted population with vanishing dipole moments. During this adiabatic following process, the actual Bloch vector deviates substantially from the instantaneous steady state, shown as the dotted (green) curve in Fig. 11(a). This is due to the reduced relaxation rate for the weaker field and the more rapid change of the instantaneous steady state in the pulse tail around the steady-state switching threshold. This departure between $\boldsymbol{\rho}(t)$ and $\boldsymbol{\rho}_{ss}^{inst}(\epsilon(t))$ is already observable at time $t_2=42.5$ ps as the deviation of $\boldsymbol{\rho}(t_2)$ from $\boldsymbol{\rho}_{ss}^{inst}(t_2)$, which is the instantaneous steady state at t_2. The departure becomes much more significant toward the end of the pulse at $t_3=60$ ps [shown as the difference between $\boldsymbol{\rho}(t_3)$ and $\boldsymbol{\rho}_{ss}^{inst}(t_3)$]. The departure of $\boldsymbol{\rho}(t)$ from $\boldsymbol{\rho}_{ss}^{inst}(\epsilon(t))$ during the adiabatic following process is a key to achieving much higher population inversion than possible in previous studies [27,28,33] of

steady-state switching. It is a striking consequence of the fact that the Bloch vector norm experiences relatively slow decay during the adiabatic following process at reduced field strength. The steady-state attraction condition [Eq. (31a)] no longer holds toward the tail of the pulse. As a result, instead of relaxing and following the evolution of the instantaneous steady state to the ground state as the pulse subsides, the Bloch vector follows the evolution of the torque vector adiabatically to achieve a highly inverted state.

Although the whole dynamical inversion process shown in Fig. 11 has a time span of 60 ps, the FWHM pulse duration is just 15 ps. The illustrative 60 ps long time duration was chosen for the purpose of showing a smooth evolution path for the quantum-dot Bloch vector. The process can actually be completed in a much shorter time scale around the pulse duration τ, with sharper pulse precursors and tails. As will be shown later, the high decay rate $\gamma_{high}=2.5$ THz in the high LDOS region enables even 1 ps pulses to achieve the dynamic inversion described above. The dynamical inversion of the quantum dot is both much faster and much larger than its steady-state counterpart [33]. The power consumption is likewise lower since we need only a short pulse to perform switching. Instead of a steady cw beam, the inverted state can be maintained by a train of picosecond pulses, separated by a time scale of $1/\gamma_+$, which can be in the range of 10–100 ps.

One significant feature of the dynamical inversion is that the initial condition of the Bloch vector $\boldsymbol{\rho}(t_0=0)$ has almost no influence on the final Bloch state achieved toward the vanishing tail of the pulse. This is a direct consequence of the steady-state attraction process, during which most of the information about the initial Bloch vector is rapidly damped out. We demonstrate this fact in Fig. 12 with the same pulse and system parameters as in Fig. 11. Figure 12 illustrates that the quantum-dot Bloch vectors can start from three different initial positions $\boldsymbol{\rho}_{1,2,3}(t_0)$, but their subsequent trajectories converge to the same peak instantaneous steady state [shown as $\boldsymbol{\rho}_{ss}^{inst}(t_1)$] at time t_1. After that, they follow the identical adiabatic path from $\boldsymbol{\rho}(t_1)$ to $\boldsymbol{\rho}(t_4)$. The different initial conditions $\boldsymbol{\rho}_{1,2,3}(t_0)$ have almost no influence on the final inverted state. This is a very important property for the application of the dynamic inversion to practical optical switches. It means that noise and fluctuations in the initial condition, as well as past operation histories, do not distort present or future optical logic operations.

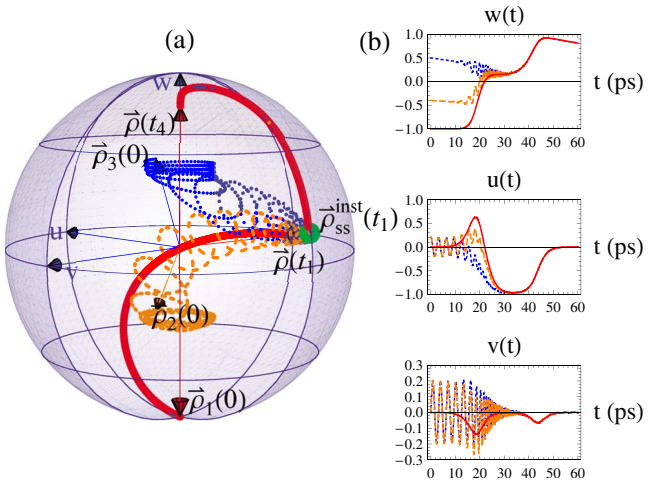

FIG. 12. (Color online) Dynamical inversion of a two-level atom with different initial conditions. $\gamma_-=2.5$ THz, $\gamma_+=5$ GHz, $\gamma_p=0$ THz, $\Delta_{LE}=1$ THz, $\Delta_{AL}=2$ THz, $\epsilon_p=6$ THz, $t_1=32.5$ ps, $t_4=60$ ps, and $\tau=15$ ps. (a) 3D evolution paths of the Bloch vector $\boldsymbol{\rho}(t)$ with initial conditions $\boldsymbol{\rho}_1(t_0=0)=(0,0,-1)$ (red solid curve), $\boldsymbol{\rho}_2(t_0)=(0.2,0,-0.4)$ (orange dashed curve), and $\boldsymbol{\rho}_3(t_0)=(0.2,0,0.5)$ (blue dotted curve); (b) 2D plot of the dipole moments $u(t)$, $v(t)$, and population inversion $w(t)$ as functions of time, with initial condition $\boldsymbol{\rho}_1(t_0)=(0,0,-1)$ (red solid curves), $\boldsymbol{\rho}_2(t_0)=(0.2,0,-0.4)$ (orange dashed curves), and $\boldsymbol{\rho}_3(t_0)=(0.2,0,0.5)$ (blue dotted curves).

C. Trade off between steady-state attraction and adiabatic following conditions

We now study the steady-state attraction condition [Eq. (31)] and the adiabatic condition [Eq. (30)] in more detail. These two conditions must be satisfied for stable dynamical inversion with the highest possible inversion allowed by $\gamma_\pm$ and γ_p. More specifically, we need the pulse to satisfy the steady-state attraction condition [Eq. (31)] for a sufficient long time duration around its peak and satisfy the adiabatic condition [Eq. (30)] throughout the second half of the pulse until its vanishing tail. Slight deviation from Eq. (30) may lead to a final inverted state with oscillating dipole moments due to possible transient oscillations that are difficult to control. Slight deviation from Eq. (31) may reduce the achievable maximum inversion as estimated in Eq. (35) because the Bloch vector does not have enough time to reach $\boldsymbol{\rho}_{ss}(\epsilon_p)$. More significant deviations from Eqs. (30) and (31) can completely destroy the dynamical inversion phenomena. We now study the major factors that affect the validity of these two conditions.

For a smooth pulse, the left-hand side of Eq. (30) can be roughly characterized as $\epsilon_p/(\tau|\Delta_{AL}|)$ with τ being the pulse duration, while the right-hand side (RHS) has $|\boldsymbol{\Omega}|\geq|\Delta_{AL}|$. Therefore a sufficient condition for Eq. (30) to be satisfied throughout the second half of the pulse (until the vanishing tail) is

$$\frac{\epsilon_p}{\tau} \ll |\Delta_{AL}|^2. \tag{33}$$

Typically for a smooth strong pulse, Eq. (31a) is more easily satisfied than Eq. (31b) because the instantaneous steady state changes very slowly around the peak: $|d\boldsymbol{\rho}_{ss}^{inst}(\epsilon)/dt|=|d\boldsymbol{\rho}_{ss}^{inst}(\epsilon)/d\epsilon||d\epsilon/dt|$. $d\epsilon/dt$ remains small near the peak of a smooth pulse and $|d\boldsymbol{\rho}_{ss}^{inst}(\epsilon)/d\epsilon|$ is small when the Rabi frequency is far above the switching threshold (see Fig. 5). Therefore, we consider only Eq. (31b). To further investigate Eq. (31b), we note that $|\boldsymbol{\Gamma}|$ depends on both the reservoir decay rates $\gamma_\pm$ and γ_p and the dressed state composition coefficients c and s, which in turn depend on ϵ_p/Δ_{AL}. For $\Delta_{AL}>0$, $|\boldsymbol{\Gamma}|$ increases with ϵ_p/Δ_{AL}. A higher γ_- value will also give a bigger overall decay rate $|\boldsymbol{\Gamma}|$ due to the enhanced spontaneous emission at the left Mollow side band.

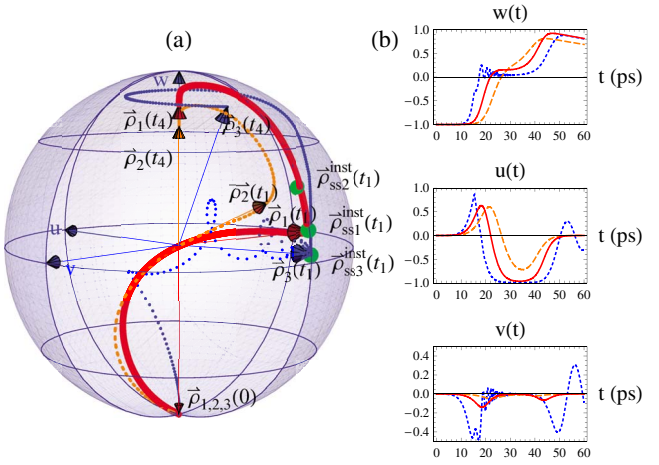

FIG. 13. (Color online) Dynamical inversion of a two-level atom with different atom-field detunings. $\gamma_-=2.5$ THz, $\gamma_+=5$ GHz, $\gamma_p=0$ THz, $\Delta_{LE}=1$ THz, $\epsilon_p=6$ THz, $t_1=32.5$ ps, $t_4=60$ ps, and $\tau=15$ ps. (a) 3D evolution paths of the Bloch vector $\boldsymbol{\rho}(t)$ with atom-field detunings $\Delta_{AL}=2$ THz (red solid curve), $\Delta_{AL}=5$ THz (orange dashed curve), and $\Delta_{AL}=0.5$ THz (blue dotted curve); (b) 2D plot of the dipole moments $u(t)$, $v(t)$, and population inversion $w(t)$ as functions of time, with atom-field detunings $\Delta_{AL}=2$ THz (red solid curves), $\Delta_{AL}=5$ THz (orange dashed curves), and $\Delta_{AL}=0.5$ THz (blue dotted curves).

γ_+ typically has little effect on $|\boldsymbol{\Gamma}|$ because it is usually much smaller than γ_- in our model. Although a high γ_p can also enhance $|\boldsymbol{\Gamma}|$ [thereby satisfying Eq. (31)], this significantly reduces the maximum inversion achievable as shown in Eq. (35). Therefore a large γ_p is not desirable. In short, for Eq. (31) to hold, a high ϵ_p/Δ_{AL} ratio and high γ_- are important.

Simply put, both the steady-state attraction condition [Eq. (30)] and the adiabatic condition [Eq. (30)] are satisfied with a strong smooth pulse with proper time duration τ and atom-field detuning Δ_{AL} and with sufficiently large decay rate γ_-. Provided these conditions are met, a Gaussian pulse shape is not necessary for the dynamic inversion to occur. Indeed, it is possible to optimize the inversion speed and switching contrast with various non-Gaussian pulses.

From the above analysis, we can also see that for a fixed photonic band-edge structure (characterized by $\gamma_\pm$) and pulse envelop (defined by τ and ϵ_p), the correct atom-field detuning Δ_{AL} is crucial for satisfying the steady-state attraction and adiabatic following conditions. The detuning determines the trade off between the two conditions when the radiative decay rates are not large compared to the pulse duration and the two conditions are not satisfied simultaneously. If Δ_{AL} is too small, the adiabatic condition may be violated according to Eq. (33). If Δ_{AL} is too large (ϵ_p/Δ_{AL} is too small), the steady-state attraction condition may be violated. Choosing Δ_{AL} in an appropriate range is important. As an example, Fig. 13 shows three different dynamical inversions for different Δ_{AL}, each starting from the ground state at $t=0$ but arriving at three different final states at t_4. In Fig. 13(a), the (red) solid evolution path of $\boldsymbol{\rho}_1$ corresponds to a properly chosen $\Delta_{AL}=2$ THz. In this case, both the steady-state attraction and adiabatic conditions are satisfied and the final state $\boldsymbol{\rho}_1(t_4)$ has a high inversion without transient dipole oscillations. The (orange) dashed evolution path of $\boldsymbol{\rho}_2$ corresponds to excessive $\Delta_{AL}=5$ THz. As a result, the steady-state attraction condition is violated and the Bloch vector cannot reach the peak instantaneous steady state shown as the dot $\boldsymbol{\rho}^{inst}_{ss2}(t_1)$ during the steady-state attraction process [$\boldsymbol{\rho}_2(t_1)$ is far away from $\boldsymbol{\rho}^{inst}_{ss2}(t_1)$]. The maximum inversion achieved by $\boldsymbol{\rho}_2$ is smaller than that of $\boldsymbol{\rho}_1$ due to the insufficient Bloch vector norm attained during the steady-state attraction process. The (blue) dotted evolution path of $\boldsymbol{\rho}_3$ corresponds to undervalued $\Delta_{AL}=0.5$ THz. In this case, the adiabatic condition is not satisfied and the evolution path shows significant transient oscillations, making the final state $\boldsymbol{\rho}_3(t_4)$ hard to control.

D. Maximum inversion: Analytical estimate

We now investigate in detail the factors that influence the final state of the Bloch vector. We are especially interested in the maximum achievable inversion when both Eqs. (30) and (31) are well satisfied. This maximum inversion typically occurs toward the end of the optical pulse interaction.

Strictly speaking, every parameter in the system has some influence on the maximum achievable inversion. This includes the decay rates $\gamma_\pm$, the dephasing rate γ_p, the atom-field detuning Δ_{AL}, the pulse peak Rabi frequency ϵ_p, and possibly the temporal profile of the pulse envelop function. But from the two-step dynamic inversion process described in Sec. V B, we find that all these factors exert their influence on the maximum achievable inversion in two basic ways. One is through their influence on the norm of the Bloch vector at the end of the steady-state attraction process. This defines the Bloch norm at the beginning of the adiabatic following process. The other is through their influence on the amount of decay experienced by the Bloch vector norm during the adiabatic following process. Once the norm of the Bloch vector (at the end of the steady-state attraction process) and the amount of decay experienced by the Bloch vector norm (during the adiabatic following process) are determined, the final norm of the Bloch vector (toward the vanishing tail of the pulse) can be predicted. Since the highly inverted state corresponds to a nearly vertical quantum-dot Bloch vector (absence of any significant polarization), the magnitude of inversion is itself nearly the norm of the Bloch vector.

The above argument can be quantified by postulating an approximate relationship,

$$w_{\max} \approx |\boldsymbol{\rho}_{w_{\max}}| \approx F_{decay}|\boldsymbol{\rho}_p|, \tag{34}$$

where $|\boldsymbol{\rho}_{w_{\max}}|$ is the Bloch vector norm at the maximum inversion point near the end of the pulse, $|\boldsymbol{\rho}_p|$ is the Bloch vector norm at the pulse peak, and F_{decay} is the effective decay factor of the Bloch norm during the adiabatic following process. If the steady-state attraction condition [Eq. (31)] is well satisfied, then $|\boldsymbol{\rho}_p| \approx |\boldsymbol{\rho}_{ss}(\epsilon_p)|$. From Eq. (27) we have $|\boldsymbol{\rho}_{ss}(\epsilon_p)| = \sqrt{u^2_{ss}(\epsilon_p)+v^2_{ss}(\epsilon_p)+w^2_{ss}(\epsilon_p)}$, which in the strong-field limit is given by $\lim_{\epsilon_p/\Delta_{AL}\to\infty}|\boldsymbol{\rho}_{ss}(\epsilon_p)| = (\gamma_- - \gamma_+)/(\gamma_- + \gamma_+ + 8\gamma_p)$. Although it is difficult to give an exact analytic expression of the amount of decay during the adiabatic following process, we can reasonably assume that it approximates

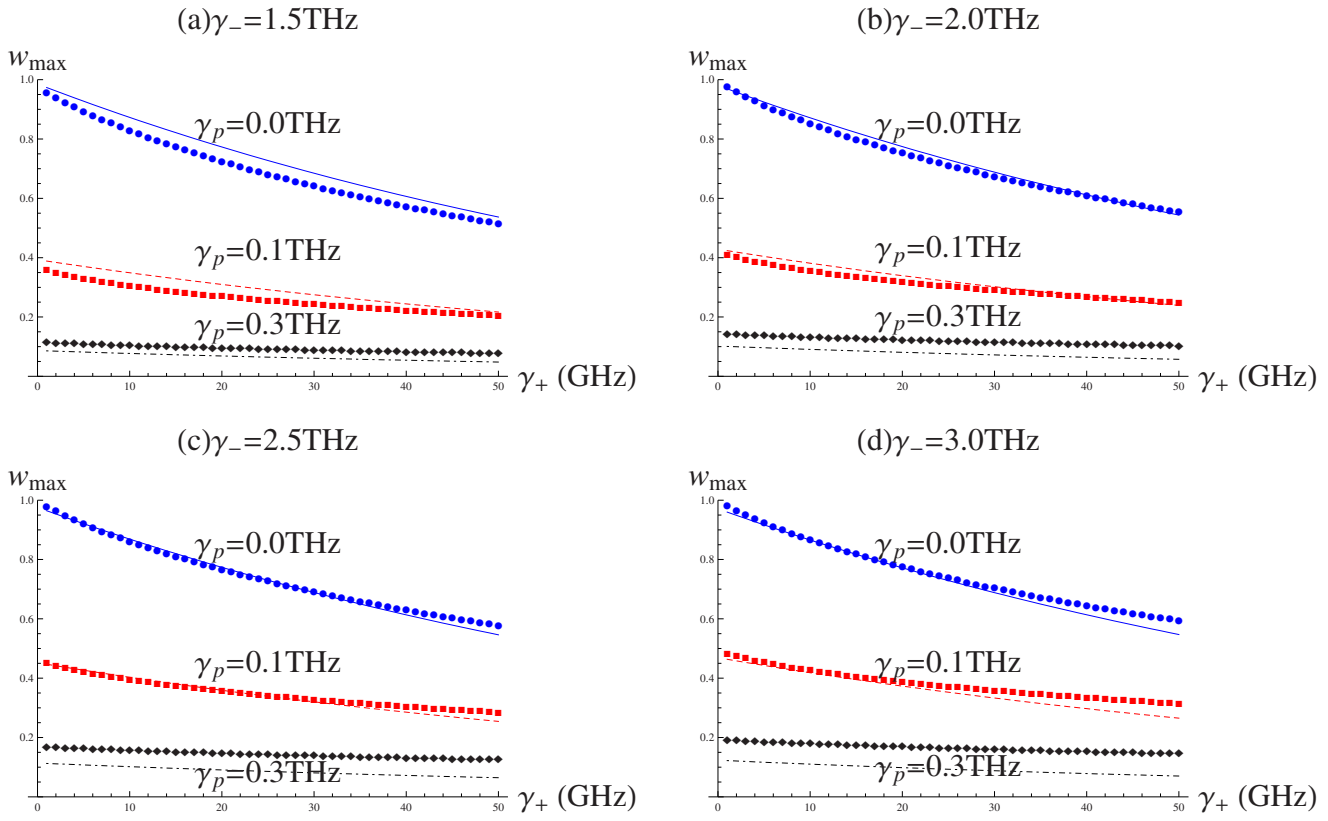

FIG. 14. (Color online) Comparison of the analytic estimation of the maximum inversion $w_{\max}$ through Eq. (35) (solid, dashed, and dotted lines) with numerical simulation results (marked curves) for different values of $\gamma_\pm$ and γ_p. The Gaussian pulse has a detuning from the atom $\Delta_{AL}=2$ THz and a detuning from the band edge $\Delta_{LE}=1$ THz, with $\epsilon_p=6$ THz and $\tau=15$ ps. The fitting parameters used are $\lambda_1 \approx 10.8$ ps, $\lambda_2 \approx 9.8\times 10^{-3}$ ps, and $\lambda_3=4.9$ ps. A total of 800 numerical simulation points are used as data. The mean regression sum of squares MSR=44.1 and the mean squared error MSE$\approx 5.3\times 10^{-4}$.

the form of an exponential function with the decay rate dependent on $\gamma_\pm$ and γ_p. So if the steady-state attraction condition is well satisfied, $w_{\max} \approx e^{-(\lambda_1\gamma_+ + \lambda_2\gamma_- + \lambda_3\gamma_p)}|\boldsymbol{\rho}_{ss}(\epsilon_p)|$, where $\lambda_{1,2,3}$ are fitting parameters with dimension of time that depend on pulse shape and duration. If furthermore, $\epsilon_p/\Delta_{AL} \gg 1$, then we can simplify $w_{\max}$ to its strong-field limit. The maximum inversion is then roughly estimated solely by the three decay rates γ_+, γ_-, and γ_p as

$$w_{\max} \approx e^{-(\lambda_1\gamma_+ + \lambda_2\gamma_- + \lambda_3\gamma_p)} \frac{\gamma_- - \gamma_+}{\gamma_- + \gamma_+ + 8\gamma_p}. \tag{35}$$

Figure 14 provides a comparison of the analytical estimate of Eq. (35) with actual numerical simulation values of $w_{\max}$. Note that all the curves in Fig. 14 are fitted as a whole, not separately, with $\gamma_\pm$ and γ_p as independent variables.

E. Rapid down switching from inverted to ground state

Up to now, we have considered dynamic inversion due to a quasisteady adiabatic pulse with $\Delta_{AL}>0$. An inverted quantum dot will remain in its excited state for a time period long compared to the switching time scale because the relaxation rate is now defined by the lower density of states in the absence of the applied field. Rapid down switching can be achieved by using another optical pulse with $\Delta_{AL}<0$. The down switching occurs, once again, via the steady-state attraction and adiabatic following processes. Consider a quasisteady adiabatic pulse with $\Delta_{AL}<0$ interacting with a two-level atom near a LDOS jump as shown schematically in Figs. 2(b) and 3(b). Unlike the system with a positive Δ_{AL}, the instantaneous steady state of the system with a negative Δ_{AL} presents no population switching. This can be verified from the analytic steady-state expression (27). As a result, during the steady-state attraction process the Bloch vector relaxes to an uninverted state well aligned with the torque vector (for $\Delta_{AL}<0$, the torque vector is always below the u-v plane). The subsequent adiabatic following process then brings the Bloch vector further downward toward the ground state. There is one subtlety for a negatively detuned pulse not present with a positively detuned pulse. While we can make $\gamma_- \equiv \gamma_{high}$ for a positively detuned pulse throughout the pulse duration by choosing $|\Delta_{AL}|>\Delta_{LE}$ [Fig. 3(a)], we cannot do this for a negatively detuned pulse impinging on a quantum dot in the low LDOS region [Fig. 3(b)]. For $\Delta_{AL}<0$, sudden changes of γ_- between γ_{low} and γ_{high} occur at the band edge. Strictly speaking, our treatment is not applicable at the immediate vicinity of ω_E. However, the duration of non-Markovian regime is very short compared with the overall pulse duration and we simply assume an instantaneous change in γ_- at ω_E. As a result, oscillations appear in the Bloch vector path when crossing jumping points of γ_-.

Figure 15(a) illustrates a typical evolution path of the Bloch vector interacting with a negatively detuned (Δ_{AL}

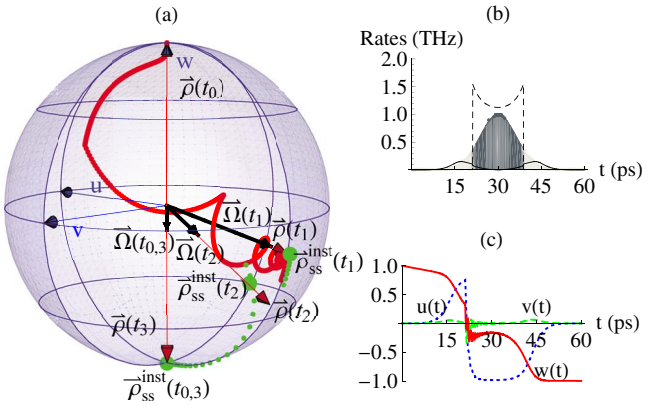

FIG. 15. (Color online) Dynamical down switching of a two-level atom to the ground state. $\gamma_{high}=2.5$ THz, $\gamma_{low}=5$ GHz, $\gamma_p=0$ THz, $\Delta_{LE}=5$ THz, $\Delta_{AL}=-2$ THz, $\epsilon_p=6$ THz, $t_c=21.17$ ps, $t_1=32.5$ ps, $t_2=40$ ps, $t_3=60$ ps, and $\tau=15$ ps. (a) 3D evolution path of the Bloch vector $\boldsymbol{\rho}(t)$ (red solid curve). The (red) thin vectors are Bloch vectors at different times, while the (black) thick vectors are the corresponding torque vectors. The big (green) dots are the instantaneous steady states at different times, while the dotted (green) curve shows the evolution path of the instantaneous steady states. (b) Scaled temporal profile of the pulse Rabi frequency, with the darkness of the shading representing how well condition [Eq. (31)] is satisfied. The solid curve is $|d\boldsymbol{\rho}_{ss}^{inst}(\epsilon(t))/dt|$ and the dashed curve is $|\boldsymbol{\Gamma}|$; all rates are in THz. (c) 2D plot of the dipole moments $u(t)$ (blue dotted curve), $v(t)$ (green dashed curve), and population inversion $w(t)$ (red solid curve) as functions of time.

<0) 15 ps quasisteady adiabatic Gaussian pulse. The quantum dot starts from a highly inverted state $\boldsymbol{\rho}(t_0)$. From $t_0=0$ ps to $t_c=21$ ps, the pulse Rabi frequency $\epsilon(t)$ grows from zero and the left Mollow sideband moves toward the LDOS jump at ω_E. But the Mollow splitting is still smaller than Δ_{LE} so that the left Mollow band remains in the low LDOS region and $\gamma_-=\gamma_+=5$ GHz. Hence the Bloch evolution from t_0 to t_c is simply that in an ordinary vacuum with vacuum decay rate γ_{low} from $\boldsymbol{\rho}(t_0)$ to $\boldsymbol{\rho}(t_c)$. For $t>t_c$, however, the left Mollow sideband enters the high LDOS region and γ_- jumps from 5 GHz to 2.5 THz. Then from t_c to $t_1=32.5$ ps, the steady-state attraction process brings the Bloch vector to $\boldsymbol{\rho}(t_1)$, very close to the instantaneous steady state $\boldsymbol{\rho}_{ss}^{inst}(t_1)$ at t_1 around the pulse peak. Now $\boldsymbol{\rho}(t_1)$ is well aligned with the torque vector $\boldsymbol{\Omega}(t_1)$ below the u-v plane. The Bloch vector then adiabatically follows $\boldsymbol{\Omega}(t)$ via $t_2=40$ ps and finally reaches the ground state at $t_3=60$ ps. Figure 15(c) shows the corresponding 2D plots of the dipole moments $u(t)$, $v(t)$, and population $w(t)$ as functions of time. The nonsmoothness of the evolution path is visible at t_c. This is an artifact of our local Markov approximation as discussed above. As in the case of dynamic inversion with a positively detuned pulse, the initial position of the Bloch vector also has almost no influence on the final state produced by this down switching process, as long as the quasisteady and adiabatic conditions [Eqs. (31) and (30), respectively] are well satisfied. The magnitude of the atom-field detuning $|\Delta_{AL}|$ is important for satisfying those conditions.

VI. APPLICATIONS OF DYNAMIC SWITCHING

Dynamic switching of driven two-level systems near a photonic band edge may have many applications. For example, population transfers (a technique, widely adopted in chemistry and molecular physics, of transferring an atom or molecule from a specified initial quantum state into a desired target state by exposing this system to a controlled pulse of radiation) [34] now rely on adiabatic inversion in ordinary vacuum through various frequency chirping techniques. In contrast, our dynamic inversion near the photonic band edge realizes inversion without frequency chirping. It also facilitates population transfers "on chip," where the two-level systems are integrated with photonic band gap materials and their population transfers are controlled on the micron scale.

In this paper, we focus on the possible application of dynamic switching to on-chip picosecond all-optical switches, operating at microwatt powers. More specifically, we aim to achieve high-contrast switching via FWHM of 1 ps pulses at high temperature (associated with a large γ_p). There are two challenges involved in this goal. The first is that at high temperature, large γ_p reduces the maximum Bloch norm attainable during the steady-state attraction process. This in turn reduces the maximum possible population inversion. We use a typical value of $\gamma_p=0.5$ THz in our study below. The second challenge comes from the use of ultrafast (picosecond) pulses. This makes it more difficult to satisfy the steady-state attraction and adiabatic conditions [Eqs. (31) and (30), respectively]. $\tau=1$ ps implies a THz rate of change of the pulse Rabi frequency. This is over ten times the rate used for the 15 ps pulse studied in earlier sections of this paper. As a result, the left-hand sides of Eqs. (31) and (30) are much larger. Therefore an increase in the atom-field detuning Δ_{AL} is necessary in order to satisfy the adiabatic condition [Eq. (30)]. Since we need to keep the ratio ϵ_p/Δ_{AL} large, we must also increase the peak Rabi frequency ϵ_p of the pulse. The steady-state attraction condition could also be satisfied by increasing the photonic decay rate γ_-. However, we face two fundamental limits in this strategy. The first is the limit of achievable γ_- defined by accuracy of fabrication of the structure. In principle the local electromagnetic density of states is divergent for an infinitely long waveguide with a mode cutoff. However imperfections in microfabrication and finite length of any practical device limit the actual magnitude of the density of states jump [9]. Although the $\gamma_-=2.5$ THz decay rate we have been using is insufficient to precisely fulfill the steady-state attraction condition [Eq. (31)], it is already larger than the THz spectral width of the pulse. Therefore, we retain the choice $\gamma_-=2.5$ THz. The second limitation is the maximum field strength that can be tolerated by our semiconductor material before dielectric breakdown occurs. This leads to an upper limit of the maximum Rabi frequency, given a specific quantum-dot transition dipole moment. [The break down field strength of GaAs is about 4×10^5 V/cm [46], while dipole moments on the order of 100 D (1 D$\approx3.335\,64\times10^{-30}$ C m) are possible in certain kind of large GaAs quantum dots [13,47,48] obtained by growth fluctuations of quantum wells as apposed to small self-assembled dots. The upper limit for Rabi frequency in such quantum-dot systems is therefore on the order of 120

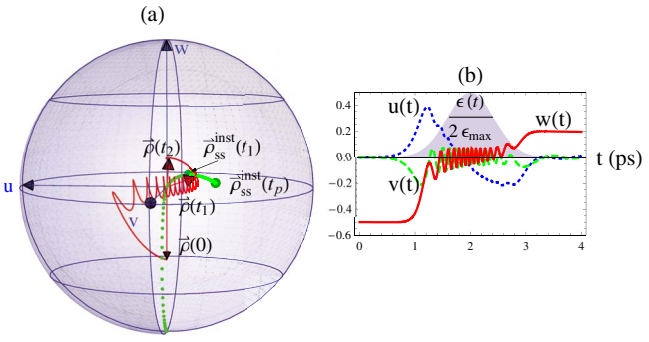

FIG. 16. (Color online) Picosecond dynamical inversion of a two-level atom. $\gamma_-=2.5$ THz, $\gamma_+=5$ GHz, $\gamma_p=0.5$ THz, $\Delta_{LE}=5$ THz, $\Delta_{AL}=8$ THz, $\epsilon_p=42$ THz, $t_p=4$ ps, $t_f=5.2$ ps, and $\tau=1$ ps. (a) 3D evolution path of the Bloch vector $\boldsymbol{\rho}(t)$ (red solid curve). The (red) thin vectors are Bloch vectors at different times. The big (green) dots are the instantaneous steady states at different times, while the dotted (green) curve shows the evolution path of the instantaneous steady states; (b) 2D plot of the dipole moments $u(t)$ (blue dotted curve), $v(t)$ (green dashed curve), and population inversion $w(t)$ (red solid curve) as functions of time.

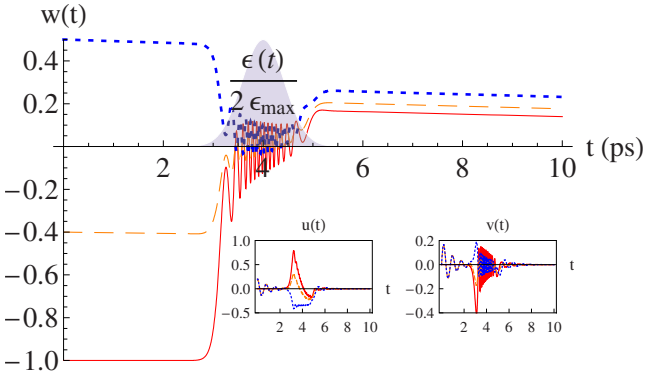

FIG. 17. (Color online) 2D plot of $u(t)$, $v(t)$, and $w(t)$ for the picosecond dynamical inversion of a two-level atom with different initial conditions. $\gamma_-=2.5$ THz, $\gamma_+=5$ GHz, $\gamma_p=0.5$ THz, $\Delta_{LE}=5$ THz, $\Delta_{AL}=8$ THz, $\epsilon_p=42$ THz, $t_p=4$ ps, and $\tau=1$ ps. Red solid curves: $\boldsymbol{\rho}(t_0=0)=(0,0,-1)$; orange dashed curves: $\boldsymbol{\rho}(t_0)=(0.2,0,-0.4)$; and blue dotted curves: $\boldsymbol{\rho}(t_0)=(0.2,0,0.5)$.

THz.] This in turn limits the maximum Δ_{AL} we can adopt since we want to keep ϵ_p/Δ_{AL} large for the steady-state attraction. Due to this limit in ϵ_p, there is a compromise between satisfying the steady-state attraction condition and the adiabatic following condition. The two factors, γ_- and ϵ_p, present practical limits to the extent to which we can satisfy both conditions [Eqs. (31) and (30)] simultaneously.

Given the above practical limits for a pulse with FWHM of 1 ps, namely, $\gamma_p=0.5$ THz, $\gamma_-=2.5$ THz, and $\epsilon_p<120$ THz, we consider different combinations of Δ_{AL} and ϵ_p in search of the best dynamic inversion performance. The steady-state attraction condition and the adiabatic following condition cannot be fulfilled simultaneously due to the practical limitation on γ_-. Instead, we seek a balance between the two. One suitable set of parameters we find is $\epsilon_p=42$ THz and $\Delta_{AL}=8$ THz. The decay rate γ_+ does not substantially modify the Bloch vector dynamics provided it remains much smaller than γ_-. We choose $\gamma_+=5$ GHz. Figure 16 shows a numerical simulation of the dynamic inversion for the above set of parameters. A final inversion around 0.2 is achieved. In Fig. 16(a), we see that the Bloch vector starts from a state below inversion $\boldsymbol{\rho}(t_0)$ and relaxes toward the instantaneous peak steady state $\boldsymbol{\rho}_{ss}^{inst}(t_p)$. Since the steady-state attraction condition [Eq. (31)] is not well satisfied, the Bloch vector fails to reach $\boldsymbol{\rho}_{ss}^{inst}(t_p)$ during the attraction process. For a picosecond pulse, the Bloch vector never reaches any instantaneous steady state [shown as the (green) dotted curve in Fig. 16(a)]. The smallest distance between the Bloch vector and the instantaneous steady states occurs around $t_1=2.8$ ps after the peak of the pulse at $t_p=2$ ps. During the adiabatic process from t_1 to $t_2=3.2$ ps, the Bloch vector does not strictly follow the movement of the torque vector. This is evident from the small transient oscillations that persist after t_2. These oscillations result from precession of the Bloch vector not well aligned with the torque vector at t_1 (the beginning of the adiabatic process). Also Δ_{AL} is not large enough to satisfy the adiabatic condition [Eq. (30)].

Since the steady-state attraction condition [Eq. (31)] is not fully satisfied for the dynamic inversion shown in Fig. 16, memory of the initial state of the Bloch vector is not completely damped out during the attraction process. Consequently, Bloch vectors starting from different positions before the pulse arrives can reach slightly different inversions after the pulse passes. This effect is shown in Fig. 17. Three different initial Bloch vector positions are considered. The dipole moments $u(t)$ and $v(t)$ all go to zero regardless of the initial conditions, but the maximum inversion achieved is different. For $\boldsymbol{\rho}(t_0=0)=(0,0,-1)$ (red solid curves), the maximum inversion is $w_{max}\approx 0.17$. For $\boldsymbol{\rho}(t_0)=(0.2,0,-0.4)$ (orange dashed curves), $w_{max}\approx 0.20$, and for $\boldsymbol{\rho}(t_0)=(0.2,0,0.5)$ (blue dotted curves), $w_{max}\approx 0.26$.

Despite the imperfect dynamic inversion for a picosecond pulse, an average inversion of about $w_{max}\approx 0.2$ is realized at a temperature corresponding to $\gamma_p=0.5$ THz. Since the final inversion varies only moderately with the initial Bloch vector state, the dynamic inversion mechanism applied to a large collection of inhomogeneously broadened quantum dots should still provide reliable picosecond switching of a waveguide segment from absorption to gain.

We propose a simple picosecond switching device based on the population flipping of two-level systems using optical pulse streams in a 3D PBG waveguide with a band edge (waveguide with cutoff mode). The inset of Fig. 20 depicts the spectral configuration of the device. It is composed of two channels of picosecond quasisteady adiabatic pulses with central frequencies ω_{L_1} for channel 1 (dark peak) and ω_{L_2} for channel 2 (light peak), interacting with a collection of inhomogeneously broadened but independent two-level atoms with average transition frequency $\bar{\omega}_A$ and standard deviation σ_A (Black peak). The LDOS of the photonic reservoir presents a sharp jump at ω_E, with decay rates γ_{high} for $\omega<\omega_E$ and γ_{low} for $\omega>\omega_E$. The device is assumed to operate in a temperature environment modeled with a rapid phonon dephasing rate γ_p. A quasisteady adiabatic pulse in channel 1 ($\bar{\Delta}_{AL_1}>0$) switches the two-level atoms to an inverted state, while a quasisteady adiabatic pulse in channel 2 ($\bar{\Delta}_{AL_2}<0$)

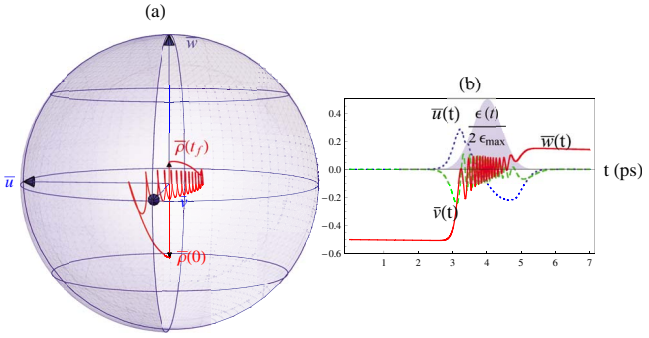

FIG. 18. (Color online) Picosecond dynamical switching of a collection of inhomogeneously broadened independent two-level atoms to a negative inversion state. $\gamma_{high}=2.5$ THz, $\gamma_{low}=5$ GHz, $\gamma_p=0.5$ THz, $\Delta_{LE}=5$ THz, $\bar{\Delta}_{AL}=8$ THz, $\Delta\omega_A=12$ THz, $\epsilon_p=42$ THz, $t_f=6$ ps, and $\tau=1$ ps. (a) 3D evolution path of the average Bloch vector $\bar{\boldsymbol{\rho}}(t)$ (red solid curve). The (red) vectors are the initial and final average Bloch vectors; (b) 2D plot of the average dipole moments $\bar{u}(t)$ (blue dotted curve), $\bar{v}(t)$ (green dashed curve), and population inversion $\bar{w}(t)$ (red solid curve) as functions of time.

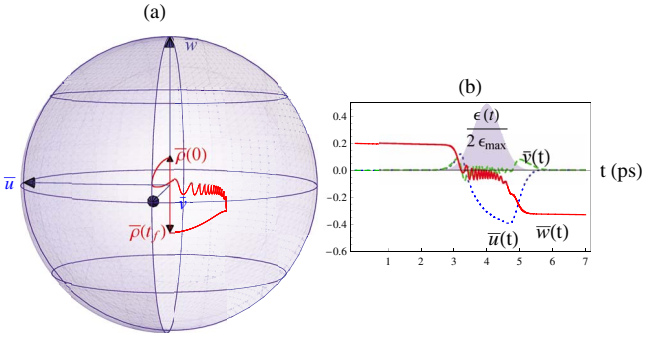

FIG. 19. (Color online) Picosecond dynamical switch of a collection of inhomogeneously broadened independent two-level atoms to a negative inversion state. $\gamma_{high}=2.5$ THz, $\gamma_{low}=5$ GHz, $\gamma_p=0.5$ THz, $\Delta_{LE}=21$ THz, $\bar{\Delta}_{AL}=-8$ THz, $\Delta\omega_A=12$ THz, $\epsilon_p=42$ THz, $t_f=6$ ps, and $\tau=1$ ps. (a) 3D evolution path of the average Bloch vector $\bar{\boldsymbol{\rho}}(t)$ (red solid curve). The (red) vectors are the initial and final average Bloch vectors; (b) 2D plot of the average dipole moments $\bar{u}(t)$ (blue dotted curve), $\bar{v}(t)$ (green dashed curve), and population inversion $\bar{w}(t)$ (red solid curve) as functions of time.

switches the two-level atoms to an uninverted state.

As an example, we choose the parameters such that the average detuning of ω_{L_1} from the two-level systems is $\bar{\Delta}_{AL_1}=8$ THz, and the average detuning of ω_{L_2} from the two-level systems is $\bar{\Delta}_{AL_2}=-8$ THz. The two-level quantum dots have a Gaussian distribution with FWHM, $\Delta\omega_A=12$ THz. (For dot transition around 1.55 μm, this corresponds to $\Delta\omega_A/\bar{\omega}_A\approx 1\%$, while for dot transition around 1.2 μm, $\Delta\omega_A/\bar{\omega}_A\approx 0.6\%$.) The detuning of channel 1 from the band edge is $\Delta_{L_1E}=5$ THz. We also choose the decay rates $\gamma_{high}=2.5$ THz, $\gamma_{low}=5$ GHz, and $\gamma_p=0.5$ THz. The pulses we are using are Gaussian in shape with FWHM duration of 1 ps and peak Rabi frequency $\epsilon_p=42$ THz. We simulate the interaction of the two-level atoms with the two channels of pulses separately in the rotating frames of ω_{L_1} and ω_{L_2} for channel 1 and channel 2, respectively.

Figure 18 shows the evolution of the weighted averages of the Bloch vector $\bar{\boldsymbol{\rho}}(t)$, as well as the dipole moments $\bar{u}(t)$, $\bar{v}(t)$, and population inversion $\bar{w}(t)$ under the interaction with a quasisteady adiabatic pulse in channel 1. The maximum inversion achieved in this simulation is $\bar{w}_{\max}\approx 0.15$, with initial position of the Bloch vector $\bar{\boldsymbol{\rho}}(t_0)=(0,0,-0.5)$. Remarkably, the transient oscillations during the adiabatic process are not averaged out, and the evolution curve of the weighted average Bloch vector closely resembles that of the Bloch vector for a single two-level atom with $\Delta_{AL}=\bar{\Delta}_{AL}$, as shown in Fig. 16.

Figure 19 shows the evolution of the weighted averages of the Bloch vector $\bar{\boldsymbol{\rho}}(t)$, as well as the dipole moments $\bar{u}(t)$, $\bar{v}(t)$, and population inversion $\bar{w}(t)$ under the interaction with a quasisteady adiabatic pulse in channel 2. The final deexcitation achieved in this simulation is $\bar{w}_{\max}\approx -0.35$, with initial position of the Bloch vector $\bar{\boldsymbol{\rho}}(t_0)=(0,0,0.2)$.

Figure 20 illustrates the continuous stable switching operations performed by this model device. The solid curve shows the time evolution of the average population inversion $\bar{w}(t)$, controlled by the pulses in channel 1 and channel 2, whose scaled temporal profiles are shown as the dark and light shaded regions in the graph, respectively. The switching action of each pulse is simulated separately, with the final state produced by the previous pulse as the initial condition of the quantum dots for the current pulse. The dipole moment components of all the final states are approximated as

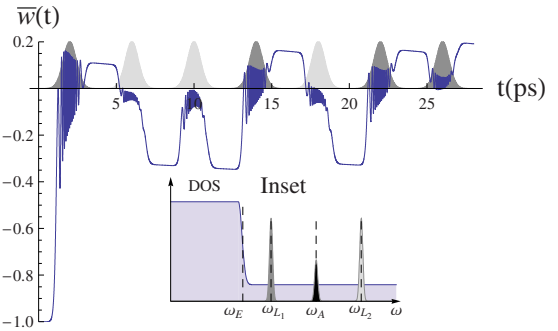

FIG. 20. (Color online) Demonstration of the high temperature operation of a possible dynamical switching device, with a collection of inhomogeneously broadened but independent two-level atoms controlled by two channels of picosecond Gaussian pulses near a photonic band edge. The optical pulse train controls the average population $\bar{w}(t)$ (solid curve) of inhomogeneously broadened atomic distribution with phonon dephasing and the scaled temporal profiles of the pulses in channel 1 (dark shading) and channel 2 (light shading). All pulses have a FWHM of $\tau=1$ ps and peak Rabi frequency $\epsilon_p=42$ THz. The switching contrast of $\bar{w}$ is about 0.5; inset: schematic spectral model of the switching device, showing the LDOS structure with a band-edge frequency ω_E, the Gaussian distribution of the inhomogeneously broadened atomic transition frequency (black shading) with mean $\bar{\omega}_A$, and the two control channels of picosecond Gaussian pulses with central frequencies ω_{L_1} (dark shading) and ω_{L_2} (light shading). The relative positions of those frequencies are specified by the detunings $\Delta_{L_1E}=5$ THz, $\bar{\Delta}_{AL_1}=8$ THz, $\bar{\Delta}_{AL_2}=-8$ THz and inhomogeneous width $\Delta\omega_A=12$ THz. The decay rates are $\gamma_{high}=2.5$ THz ($\gamma_{high}^{-1}=0.4$ ps), $\gamma_{low}=0.005$ THz, and $\gamma_p=0.5$ THz.

zero for simplicity. The separation between two consecutive pulses is 4 ps but can be made much longer with essentially the same result. A switching contrast of about 0.5 is achieved.

After the passage of a control pulse in channel 1, although the instantaneous steady state $\boldsymbol{\rho}_{ss}^{inst}$ immediately returns to the ground state, the true atomic population $\bar{w}$ stays inverted with slow decay rate γ_{low}. If a subsequent weak signal pulse (with area π) in a third resonant channel (centered at $\bar{\omega}_A$) passes through this amplifying medium, pulse transmission and reshaping are equivalent to that of an amplifying medium in ordinary vacuum [19,49] (provided the signal pulse is not so strong to push the Mollow sidebands back into the high LDOS region). With an additional broadband linear loss, weak signal pulses will be amplified into stable π pulse solitons and traverse the device without attenuation. On the other hand, a control pulse in channel 2 leaves $\bar{w}$ uninverted. Under the action of this resonant medium alone, according to the McCall-Hahn area theorem [19,20], a subsequent signal π pulse is at the unstable branch point where it can be either amplified to area 2π or completely absorbed during propagation. But the presence of the additional broadband linear loss pushes the pulse into the absorption branch, leading to complete absorption of the signal pulse. Effectively, we can control light (signal pulses in channel 3) with light (femtojoule control pulses in channels 1 and 2) on picosecond time scales with microwatt average power levels (to be estimated below).

To estimate the energy per control pulse and the average operating power of the proposed all-optical switch device, assume the pulse is in the propagating mode of a 3D-2D heterostructure similar to the "architecture 1" in Ref. [33], with a 2D layer lattice constant $a=0.425$ μm for 1.55 μm central vacuum wavelength. The height of the 2D layer is assumed to be $h=0.3a$. We assume that the field strength envelop function has a Gaussian temporal profile with FWHM $W_t=1$ ps and a Gaussian spatial cross sectional profile along the in-plane normal direction (x direction) of the waveguide (along y direction) with FWHM $W_x=a$ and is uniform along the out-of-plane normal direction (z direction) within the 2D layer but vanishes abruptly at the 3D PBG cladding boundary (i.e., a step profile in the z direction). The peak field strength is $|\mathcal{E}_p|=1.4\times10^7$ V/m according to the parameters used in the model device. So the cross section electric field strength function can be written as

$$|\mathcal{E}(t,x,z)| = |\mathcal{E}_p| e^{-4\ln 2(t/W_t)^2} e^{-4\ln 2(x/W_x)^2} f(z),$$

where $f(z)=1$ for $0<z<h$ and $f(z)=0$ otherwise.

To estimate the time-averaged Poynting vector over an optical cycle inside the waveguide, we ignored the effects of the small defect pillars and embedded two-level quantum dots on the energy density inside the waveguide by approximating the PC waveguide as an ordinary hollow dielectric waveguide with the same group velocity as the propagating mode of the PC waveguide. Then the time-averaged energy density over an optical cycle $\langle u\rangle=(\epsilon_0|\mathcal{E}|^2+|\mathcal{B}|^2/\mu_0)/4$ inside the waveguide can be estimated as $\langle u\rangle \approx \epsilon_0|\mathcal{E}(t,x,z)|^2/2$ by using the approximate plane wave relation between magnetic field and electric filed $|\mathcal{B}|=|\mathcal{E}|/c$, where ϵ_0 is the vacuum permittivity, μ_0 is the vacuum permeability, and c is the speed of light. The time-averaged Poynting vector over an optical cycle is calculated as $\langle S\rangle=\langle u\rangle v_g$, with the group velocity $v_g=0.2c$ as in Ref. [33]. Now the energy per pulse can be estimated to be

$$E = \int_{-\infty}^{\infty} dt \int_{-\infty}^{\infty} dx \int_{-\infty}^{\infty} dz \langle S\rangle \approx 1.6 \text{ fJ}.$$

The average operating power is inversely proportional to the separation time Δt between control pulses. As long as Δt is small compared with the free decay time $1/\gamma_+=200$ ps of the quantum dots in the absence of control pulses, the population inversion generated from the previous control pulse would be maintained before the next control pulse arrives. Using $\Delta t=50$ ps, the average operation power $p=E/\Delta t \approx 30$ μW, considerably below the operation power for the steady-state switching proposed earlier [33].

VII. CONCLUSION

In conclusion, we have demonstrated the consequences of two fundamentally new features of nonlinear optical Bloch vector dynamics in the presence of sharp and abrupt structure in electromagnetic density of states. The modifications of the Bloch vector equation include (i) a "vacuum structure" term proportional to the jump in the electromagnetic LDOS when the jump lies in a frequency interval less than the Rabi frequency of the light-matter interaction and (ii) remarkable field-dependent spontaneous emission and polarization relaxation rates as the atomic Mollow components span low and high electromagnetic DOS regions during interaction with an optical pulse. The vacuum structure term drives the atomic Bloch vector to a weakly inverted state in the steady-state limit. However, during interaction with a short optical pulse, the instantaneous (actual) Bloch vector adiabatically follows the pulse torque vector (in nearly antiparallel alignment) and lags considerably behind its steady-state value as the pulse amplitude rises. As the pulse approaches its peak value, the dressed atom experiences the high LDOS region and the relaxation rate of the instantaneous Bloch vector to its steady-state value is greatly enhanced. This allows the actual Bloch vector to rapidly catch up to its weakly inverted steady-state value. In doing so, the true Bloch vector rapidly switches from antiparallel to parallel alignment with the pulse torque vector. As the optical pulse amplitude subsides, the steady-state Bloch vector returns to the ground state, but the instantaneous (true) Bloch vector is unable to relax rapidly toward it since the dressed atom now probes the low LDOS part of the spectrum. Instead, the actual Bloch vector adiabatically follows the pulse torque vector (parallel alignment) to a nearly completely inverted state. This high inversion state persists long after the optical pulse subsides since the time scale of spontaneous emission in the low LDOS region is much longer than the picosecond pulse duration.

The remarkable nonlinear dynamics and population flipping of the quantum-dot Bloch vector is a direct consequence of two fundamental properties of a waveguide in a 3D PBG

material. The first property is the very strong light localization (mode confinement) of the PBG waveguide enabling very strong fields to be delivered to the location of a suitably embedded quantum dot with only modest (microwatt) power levels. Combined with the large quantum-dot transition dipole moment, this allows the separation of Mollow components in the dressed atoms to reach unprecedented values, exceeding a 1% inhomogeneously broadened spectrum of a collection of quantum dots. The second property is the unique nature of the structured electromagnetic vacuum in 3D PBG bimodal waveguide. Contrary to common expectation, the LDOS within the PBG waveguide can be several orders of magnitude larger than in ordinary vacuum. The very dense mode continuum enables radiative relaxation effects to occur on picosecond time scales, enabling them to supercede phonon-mediated relaxation events. The very precipitous jump in the electromagnetic DOS at the waveguide cutoff frequency is likewise a unique consequence of the surrounding 3D PBG. The magnitude and the spectral range of the DOS jump associated with the waveguide cutoff are determined by the length of the waveguide segment and the degree of random disorders in the PC. As an example, it has been shown in [10] that the LDOS peak of a 12-μm-long W1 PC waveguide (see [10] for detailed structure) is relatively robust to a 4% disorder ($\sim$9 nm diameter randomness for a waveguide operating at $\lambda \approx 1.5$ μm) in the dielectric rod radius outside the defect line of the waveguide, while more precise control of the defect line fabrication accuracy is required to obtain a precisely located LDOS peak within 0.3% of the operating frequency. Nonetheless, the effect of the LDOS peak location uncertainty on dynamic switching can partly be compensated by inhomogeneous broadening in the transition frequency of the quantum dots embedded in the waveguide.

Earlier strong-coupling experiments have focused on GaAs based quantum dots that emit close to 1 μm [13,15,17]. Strong coupling was also observed in a 2D PC membrane cavity at 1.2 μm using an InAs-GaAs quantum-dot system [12]. The direct application of our numerical results to these systems corresponds to a choice of inhomogeneous broadening of about 0.6% of the average transition frequency $\bar{\omega}_A$. Larger broadening, at these wavelengths, requires the use of stronger optical pulses. Strong coupling has yet to be observed experimentally at 1.55 μm in InAs-InP quantum-dot systems (for which our simulations with 1% of $\bar{\omega}_A$ broadening apply without modification). However, in a 3D PBG waveguide structure, much smaller mode volumes and larger field strengths can be achieved than in past experiments. This extraordinarily strong light localization may enable ultrafast population switching to be achieved at 1.55 μm even at room temperature. Our model is readily adapted, nevertheless, to a variety of quantum-dot systems at various wavelengths.

The dynamic population switching of quantum dots enabled by a 3D PBG waveguide enables multichannel all-optical information processing on a chip. Our integrated all-optical switching device utilizes two channels of picosecond pulses oppositely detuned from an inhomogeneously broadened two-level medium to control a third channel of on resonant picosecond signal pulses. The switching action is due to the abrupt jump of the LDOS provided by one waveguide cutoff mode. The picosecond switching time scale and the robustness to phonon-mediated relaxation are direct consequences of strong light localization and the giant Purcell factor near the cutoff point. The subwavelength confinement of light in the 3D PBG waveguide, the pulsed control beam, and the persistence of quantum-dot inversion between control pulses facilitate microwatt operating powers with only femtojoule energies required per switch. These features are important to enabling all-optical transistors to be competitive with their electronic counterpart.

ACKNOWLEDGMENTS

We are grateful to Dr. Dragan Vujic and Dr. Rongzhou Wang for some helpful discussions. This work was supported in part by the Natural Sciences and Engineering Research Council of Canada, the Canadian Institute for Advanced Research, and the Ontario Premier's Platinum Research Fund.

APPENDIX A: GENERAL FORM OF THE MASTER EQUATION

In this appendix we derive the general form of the master equation obeyed by the reduced density operator in the Born approximation when the driving beam is a time-dependent pulse.

Substituting the formal solution of Eq. (9), $\tilde{\chi}_I(t)=\tilde{\chi}_I(0)+(1/i\hbar)\int_0^t dt'[\tilde{H}_I(t'),\tilde{\chi}_I(t')]$, back into the first term on the right-hand side (RHS) of Eq. (9) [we keep the second term on the RHS of Eq. (9) in its current form and will show it disappears when transferred back into the bare atomic basis and Schrödinger picture] gives

$$\dot{\tilde{\chi}}_I(t) = \frac{1}{i\hbar}[\tilde{H}^I_{SR},\tilde{\chi}_I(0)] - [UB\dot{B}^\dagger U^\dagger,\tilde{\chi}_I(t)] - \frac{1}{\hbar^2}\int_0^t dt'[\tilde{H}^I_{SR}(t),[\tilde{H}_I(t'),\tilde{\chi}_I(t')]]. \quad \text{(A1)}$$

Assume that the interaction between the atomic system and the reservoir is turned on at $t=0$ with no correlation between the two at that moment, so that $\tilde{\chi}_I(0)=\tilde{\varrho}_I(0)R_0$. Here, $\tilde{\varrho}_I$ is the reduced density operator of the atomic system under dressed state basis and in the interaction picture, while R_0 is the density operator of the reservoir at $t=0$. Also assume the reservoir to be at thermal equilibrium so that R_0 is diagonal, then we have

$$\langle a_\lambda\rangle_R = \langle a^\dagger_\lambda\rangle_R = 0. \quad \text{(A2)}$$

As a result, the first term in Eq. (A1) becomes zero because $\mathrm{Tr}_R[\tilde{H}^I_{SR}(t)R_0]=0$. Under these assumptions, we can obtain the formal equation of motion of the reduced density operator by taking the trace over the reservoir degree of freedom in Eq. (A1),

$$\dot{\tilde{\varrho}}_I(t) = -\frac{1}{\hbar^2}\int_0^t dt'\ \mathrm{Tr}_R\{[\tilde{H}^I_{SR}(t),[\tilde{H}^I_{SR}(t'),\tilde{\chi}_I(t')]]\} + \frac{i}{\hbar}\int_0^t dt'\ \mathrm{Tr}_R\{[\tilde{H}^I_{SR}(t),[UB\dot{B}^\dagger U^\dagger(t'),\tilde{\chi}_I(t')]]\} - \mathrm{Tr}_R[UB\dot{B}^\dagger U^\dagger(t),\tilde{\chi}_I(t)]. \quad \text{(A3)}$$

The standard Born approximation assumes weak coupling between the atomic system and the reservoir during the time evolution so that $\tilde{\chi}_I(t)=\tilde{\varrho}_I(t)R_0+O(\tilde{H}^I_{SR})$. Keeping only up to the second order in $\tilde{H}^I_{SR}$ in Eq. (A3), the master equation now becomes

$$\dot{\tilde{\varrho}}_I(t) = [\dot{\tilde{\varrho}}_I]_1 + [\dot{\tilde{\varrho}}_I]_2 - \mathrm{Tr}_R[UB\dot{B}^\dagger U^\dagger(t),\tilde{\chi}_I(t)] \quad \text{(A4)}$$

with the two integral terms,

$$[\dot{\tilde{\varrho}}_I]_1 = -\frac{1}{\hbar^2}\int_0^t dt'\ \mathrm{Tr}_R\{[\tilde{H}^I_{SR}(t),[\tilde{H}^I_{SR}(t'),\tilde{\varrho}_I(t')R_0]]\},$$

$$[\dot{\tilde{\varrho}}_I]_2 = \frac{i}{\hbar}\int_0^t dt'\ \mathrm{Tr}_R\{[\tilde{H}^I_{SR}(t),[UB\dot{B}^\dagger U^\dagger(t'),\tilde{\varrho}_I(t')R_0 + O(\tilde{H}^I_{SR})]]\}. \quad \text{(A5)}$$

The standard Markovian approximation assumes that the future evolution of $\tilde{\varrho}_I(t)$ does not depend on its past values, so that $\tilde{\varrho}_I(t')$ is replaced by $\tilde{\varrho}_I(t)$ on the RHS of Eq. (A4). By writing $\tilde{H}^I_{SR}$ in the form $\tilde{H}^I_{SR}=\Sigma_i \tilde{S}_i\tilde{\Gamma}_i$, then after the Born-Markov approximation, the first integral term becomes

$$[\dot{\tilde{\varrho}}_I]_1 = -\sum_{i,j}\frac{1}{\hbar^2}\int_0^t dt'\{[\tilde{S}_i\tilde{S}_j\tilde{\varrho}_I(t)-\tilde{S}_j\tilde{\varrho}_I(t)\tilde{S}_i]\langle\tilde{\Gamma}_i(t)\tilde{\Gamma}_j(t')\rangle_R + [\tilde{\varrho}_I(t)\tilde{S}_j\tilde{S}_i-\tilde{S}_i\tilde{\varrho}_I(t)\tilde{S}_j]\langle\tilde{\Gamma}_j(t')\tilde{\Gamma}_i(t)\rangle_R\}, \quad \text{(A6)}$$

where $\langle\tilde{\Gamma}_i(t)\tilde{\Gamma}_j(t')\rangle_R=\mathrm{Tr}_R[\tilde{R}_0\tilde{\Gamma}_i(t)\tilde{\Gamma}_j(t')]$, $\tilde{\varrho}_I(t)$ is the reduced density operator of the atom, and $\tilde{R}_0$ is the reservoir part of the density operator.

Now let us look at the second integral term $[\dot{\tilde{\varrho}}_I]_2$ in Eq. (A4),

$$[\dot{\tilde{\varrho}}_I]_2 = \frac{i}{\hbar}\int_0^t dt'\ \mathrm{Tr}_R\{[\tilde{H}^I_{SR}(t),[UB\dot{B}^\dagger U^\dagger(t'),\tilde{\varrho}_I(t')R_0 + O(\tilde{H}^I_{SR})]]\} = \frac{i}{\hbar}\int_0^t dt'[\mathrm{Tr}_R\{\tilde{H}^I_{SR}(t)R_0\},[UB\dot{B}^\dagger U^\dagger(t'),\tilde{\varrho}_I(t')]] + \frac{i}{\hbar}\int_0^t dt'\ \mathrm{Tr}_R\{[\tilde{H}^I_{SR}(t),[UB\dot{B}^\dagger U^\dagger(t'),O(\tilde{H}^I_{SR})]]\}. \quad \text{(A7)}$$

For thermal equilibrium state of the reservoir, R_0 is diagonal so that $\mathrm{Tr}_R\{\tilde{H}^I_{SR}(t)R_0\}=0$ because of Eq. (A2). Physically, this is because the average of the fluctuating electric field in the reservoir is zero. Now $[\dot{\tilde{\varrho}}_I]_2$ becomes

$$[\dot{\tilde{\varrho}}_I]_2 = \frac{i}{\hbar}\int_0^t dt'\ \mathrm{Tr}_R\{[\tilde{H}^I_{SR}(t),[UB\dot{B}^\dagger U^\dagger(t'),O(\tilde{H}^I_{SR})]]\}. \quad \text{(A8)}$$

The term $UB\dot{B}^\dagger U^\dagger$ in the inner commutator characterizes the change rate of the dressed state basis. We can write the dressed state coefficients $c=\cos\theta$ and $s=\sin\theta$ with $\theta=\sin^{-1}\sqrt{(2\Omega-\Delta_{AL})/(4\Omega)}$ so that the basis transformation operators can be written as $B=B(\theta)$ and $B^\dagger=B^\dagger(\theta)$. The unitary operator $B(\theta)$ can be explained as a rotation operator that rotates any state vector by angle θ while keeping the norm unchanged. It then follows $\dot{B}^\dagger=\dot{\theta}B^\dagger(\theta+\pi/2)$. From $\sin 2\theta=2\epsilon/\sqrt{\Delta^2_{AL}+4\epsilon^2}$ we can see that the angle θ is in fact half the angle between the torque vector $\mathbf{\Omega}$ and the vertical w axis, as will be introduced later in the Bloch equation section. Thus $\dot{\theta}$ represents half the angular speed of the torque vector $\mathbf{\Omega}$. The $O(\tilde{H}^I_{SR})$ term represents the part of the overall density operator $\tilde{\chi}^{correl}_I$ that is due to correlation between the dressed system and the reservoir. More precisely, $\tilde{\chi}^{correl}_I \sim O(\tau_c\tilde{H}^I_{SR}\tilde{\varrho}_I/\hbar)$, where τ_c is the correlation time of the reservoir assumed to be much smaller than all other time scales of the system [50]. Now the order of magnitude of the contribution from Eq. (A8) toward the overall master equation is approximately

$$[\dot{\tilde{\varrho}}_I]_2 \sim -\frac{\dot{\theta}\tau_c}{\hbar^2}\int_0^t dt'\langle\tilde{H}^I_{SR}(t)\tilde{H}^I_{SR}(t')UB(\theta)B^\dagger(\theta+\pi/2)U^\dagger(t')\rangle_R\tilde{\varrho}_I(t). \quad \text{(A9)}$$

Following similar steps as when we evaluated the correlation integrals in Appendix B, in the strong-field limit, the order of magnitude of the rate of variation associated with Eq. (A9) is $O(\tau_c\dot{\theta}\gamma_-)$. If we assume that the angular speed of the torque vector $\mathbf{\Omega}$ is on the same order as the high decay rate γ_- (consistent with the time regime we are working in, i.e., the duration of the pulse is comparable with the decay time of the system), then $\dot{\theta}\sim O(\gamma_-)$, so that the order of magnitude of the rate of variation associated with Eq. (A9) becomes $O(\tau_c\gamma_-^2)$. Clearly there are two reasons to ignore the contribution of $[\dot{\tilde{\varrho}}_I]_2$ to the master equation. (i) The decay rate γ_- characterizes the intensity of the coupling described by the interaction Hamiltonian $\tilde{H}^I_{SR}$ so that $\int_0^t dt'\langle\tilde{H}^I_{SR}(t)\tilde{H}^I_{SR}(t')\rangle/\hbar^2\sim O(\gamma_-)$. Then, the $[\dot{\tilde{\varrho}}_I]_2$ term is effectively of fourth order in $\tilde{H}^I_{SR}$. Since the Born approximation keeps only up to the second order in $\tilde{H}^I_{SR}$, we can safely ignore the $[\dot{\tilde{\varrho}}_I]_2$ term. (ii) The smallness of the reservoir correlation time τ_c also suggests the $[\dot{\tilde{\varrho}}_I]_2$ term can be dropped.

Now the radiative part of the master equation in the dressed state basis and interaction picture simplifies to

$$\dot{\tilde{\varrho}}_I = [\dot{\tilde{\varrho}}_I]_1 - \mathrm{Tr}_R[UB\dot{B}^\dagger U^\dagger(t),\tilde{\chi}_I(t)] \quad \text{(A10)}$$

with

$$[\dot{\tilde{\varrho}}_I]_1 = -\sum_{i,j}\frac{1}{\hbar^2}\int_0^t dt'\{[\tilde{S}_i\tilde{S}_j\tilde{\varrho}_I(t) - \tilde{S}_j\tilde{\varrho}_I(t)\tilde{S}_i]\langle\tilde{\Gamma}_i(t)\tilde{\Gamma}_j(t')\rangle_R + [\tilde{\varrho}_I(t)\tilde{S}_j\tilde{S}_i - \tilde{S}_i\tilde{\varrho}_I(t)\tilde{S}_j]\langle\tilde{\Gamma}_j(t')\tilde{\Gamma}_i(t)\rangle_R\}. \quad \text{(A11)}$$

APPENDIX B: DRESSED ATOM CORRELATIONS IN THE LOCAL MARKOV APPROXIMATION

In this Appendix, we evaluate the integrals of each term contained in Eq. (12) for different values of i and j.

For $i=4$, $j=1$,

$$\int_0^t d\tau\langle\tilde{\Gamma}_4(t)\tilde{\Gamma}_1(t-\tau)\rangle_R = \hbar^2 c(t)s(t)\sum_\lambda |g_\lambda|^2\int_0^t d\tau c(t-\tau)s(t-\tau)e^{-i\Delta_\lambda\tau}. \quad \text{(B1)}$$

In Markovian approximation, the upper limit of the τ integral in Eq. (B1) can be extended to ∞, then by making use of Eq. (13) and the following relation with the principle value part discarded,

$$\lim_{t\to\infty}\int_0^t d\tau e^{-i\omega_L\tau} = \pi\delta(\omega_L) - i\frac{PV}{\omega_L}, \quad \text{(B2)}$$

we get

$$\int_0^t d\tau\langle\tilde{\Gamma}_4(t)\tilde{\Gamma}_1(t-\tau)\rangle_R = \frac{\hbar^2}{2}c(t)s(t)\frac{1}{\sqrt{2\pi}}\int_{-\nu_{cs}/2}^{\nu_{cs}/2} d\nu c s_\nu e^{i\nu t}\gamma_{\omega_L-\nu}, \quad \text{(B3)}$$

where $\gamma_{\omega_L-\nu}=2\pi\Sigma_\lambda|g_\lambda|^2\delta(\omega_\lambda-[\omega_L-\nu])$. If we assume that the photonic density of states is smooth during the region $[\omega_L-\nu_{cs}/2,\omega_L+\nu_{cs}/2]$ such that $\gamma_{\omega_L-\nu}\approx\gamma_{\omega_L}\equiv\gamma_0$ for $-\nu_{cs}/2\le\nu\le\nu_{cs}/2$, then using Eq. (13) reversely in Eq. (B3), we arrive at

$$\int_0^t d\tau\langle\tilde{\Gamma}_4(t)\tilde{\Gamma}_1(t-\tau)\rangle_R \approx \frac{\hbar^2}{2}c^2(t)s^2(t)\gamma_0. \quad \text{(B4)}$$

Effectively, we have made a "local Markovian" approximation around the central Mollow band located at ω_L. As long as the central Mollow band is far enough from the band edge such that the edge ω_E is outside the spectral width ν_{cs} around the central Mollow band, this approximation should be reasonable.

For $i=5$, $j=2$,

$$\int_0^t d\tau\langle\tilde{\Gamma}_5(t)\tilde{\Gamma}_2(t-\tau)\rangle_R = \hbar^2c^2(t)\sum_\lambda|g_\lambda|^2\int_0^t d\tau c^2(t-\tau)e^{-i[\Delta_\lambda-2\Omega(t)]t}\times e^{i[\Delta_\lambda-2\Omega(t-\tau)](t-\tau)}. \quad \text{(B5)}$$

Under Markovian approximation, we can replace $\Omega(t-\tau)$ with $\Omega(t)$ in the τ integration. Then by using Eq. (13), we get

$$\int_0^t d\tau\langle\tilde{\Gamma}_5(t)\tilde{\Gamma}_2(t-\tau)\rangle_R \approx \hbar^2c(t)^2\int_{-\nu_{c^2}/2}^{\nu_{c^2}/2} d\nu c_\nu^2 e^{i\nu t}\sum_\lambda|g_\lambda|^2\int_0^t d\tau e^{-i\nu\tau-i[\Delta_\lambda-2\Omega(t)]\tau}. \quad \text{(B6)}$$

By extending the τ integral to infinity and discarding the principal value part of the integration, we get

$$\int_0^t d\tau\langle\tilde{\Gamma}_5(t)\tilde{\Gamma}_2(t-\tau)\rangle_R \approx \frac{\hbar^2}{2}c(t)^2\int_{-\nu_{c^2}/2}^{\nu_{c^2}/2} d\nu c_\nu^2 e^{i\nu t}2\pi\sum_\lambda|g_\lambda|^2\delta[\omega_\lambda-\omega_L-2\Omega(t)+\nu] \approx \frac{\hbar^2}{2}c(t)^4\gamma_+, \quad \text{(B7)}$$

where $\gamma_+=2\pi\Sigma_\lambda|g_\lambda|^2\delta[\omega_\lambda-\omega_L-2\Omega(t)]\approx 2\pi\Sigma_\lambda|g_\lambda|^2\delta[\omega_\lambda-\omega_L-2\Omega(t)+\nu]$ for $\nu\in[-\nu_{c^2}/2,\nu_{c^2}/2]$ uses the local Markovian approximation around the right Mollow side band located at $\omega_L+2\Omega(t)$, just as what we have done in obtaining Eq. (B4).

Following the same steps for other combinations of i,j in Eq. (12), we obtain Eq. (14) given in the main text.

APPENDIX C: DERIVATION OF THE BLOCH EQUATION

The Bloch equation describes the temporal evolution of the atomic system under the interaction with external driving fields and dissipating environments. It is the equation of motion for the expectation values of the atomic dipole moment operators σ_1 and σ_2 and population difference operator σ_3. Because these bare atomic operators are time independent in the Schrödinger picture and bare atomic basis, the dynamics of their expectation values are solely determined by the master equation [Eq. (23)] that describes the temporal evolution of the atomic quantum states,

$$\frac{d}{dt}\langle\sigma_i\rangle = \frac{d}{dt}\mathrm{Tr}[\varrho\sigma_i] = \mathrm{Tr}[\dot{\varrho}\sigma_i]. \quad \text{(C1)}$$

Substituting Eq. (23) into Eq. (C1) for $i=1,2,3$ leads to the Bloch component equations Eq. (25) after some tedious but straight forward algebras.

We take the equation of motion for $\langle\sigma_1\rangle$ as an example,

$$\frac{d}{dt}\langle\sigma_1\rangle = -i\Omega\ \mathrm{Tr}[R_3\varrho\sigma_1] - \frac{\gamma_0 c^2 s^2 + \gamma_p (c^2 - s^2)^2}{2}[\mathrm{Tr}(\varrho\sigma_1) - \mathrm{Tr}(R_3\varrho R_3\sigma_1)] - \frac{\gamma_+ c^4 + 4\gamma_p c^2 s^2}{2}[\mathrm{Tr}(R_{22}\varrho\sigma_1) - \mathrm{Tr}(R_{12}\varrho R_{21}\sigma_1)]$$
$$- \frac{\gamma_- s^4 + 4\gamma_p c^2 s^2}{2}[\mathrm{Tr}(R_{11}\varrho\sigma_1) - \mathrm{Tr}(R_{21}\varrho R_{12}\sigma_1)] - \frac{cs}{2}\{s^2\gamma_0[\mathrm{Tr}(R_{12}\varrho\sigma_1) - \mathrm{Tr}(R_3\varrho R_{12}\sigma_1)] + c^2\gamma_+[\mathrm{Tr}(R_{12}\varrho\sigma_1)$$
$$+ \mathrm{Tr}(R_{12}\varrho R_3\sigma_1)] + s^2\gamma_-[\mathrm{Tr}(\varrho R_{12}\sigma_1) - \mathrm{Tr}(R_3\varrho R_{12}\sigma_1)] + c^2\gamma_0[\mathrm{Tr}(\varrho R_{12}\sigma_1) + \mathrm{Tr}(R_{12}\varrho R_3\sigma_1)]\} - \frac{c^2 s^2}{2}(\gamma_-$$
$$+ \gamma_+)\mathrm{Tr}[R_{21}\varrho R_{21}\sigma_1] + \mathrm{H.c.} \tag{C2}$$

To simplify Eq. (C2), we first seek the expression of the dressed state atomic operators $R_{i,j}$ $(i,j=1,2)$ and R_3 in the bare atomic basis. From Eq. (24) we can solve for σ_{21} and σ_{12},

$$\sigma_{21} = \sigma_{12}^\dagger = \tfrac{1}{2}(\sigma_1 + i\sigma_2). \tag{C3}$$

Substituting Eq. (C3) back into Eq. (21) gives

$$R_{12} = R_{21}^\dagger = cs\sigma_3 + \frac{c^2 - s^2}{2}\sigma_1 + \frac{i}{2}\sigma_2,$$

$$R_3 = (c^2 - s^2)\sigma_3 - 2cs\sigma_1 + 1,$$

$$R_{22} = \frac{1}{2}(1 + R_3) = \frac{c^2 - s^2}{2}\sigma_3 - cs\sigma_1 + \frac{1}{2},$$

$$R_{11} = \frac{1}{2}(1 - R_3) = -\frac{c^2 - s^2}{2}\sigma_3 + cs\sigma_1 - \frac{1}{2}. \tag{C4}$$

Now substitute Eq. (C4) into Eq. (C2). Then by making use of the cyclic property of trace and the fact that σ_i are Pauli matrices in the bare atomic basis, we can finally get the equation of motion for $\langle\sigma_1\rangle$. We take the first term in Eq. (C2) as an example,

$$-i\Omega\ \mathrm{Tr}[R_3\varrho\sigma_1] = -i\Omega\ \mathrm{Tr}[\varrho\sigma_1 R_3] = -i\Omega\ \mathrm{Tr}\{\varrho\sigma_1[(c^2 - s^2)\sigma_3 - 2cs\sigma_1 + 1]\} = -i(c^2 - s^2)\Omega\ \mathrm{Tr}[\varrho\sigma_1\sigma_3] + 2ics\Omega\ \mathrm{Tr}[\varrho\sigma_1\sigma_1] - i\Omega\ \mathrm{Tr}[\varrho\sigma_1] = (s^2 - c^2)\Omega\langle\sigma_2\rangle + 2ics\Omega - i\Omega\langle\sigma_1\rangle = -\frac{1}{2}\Delta_{AL}\langle\sigma_2\rangle + 2ics\Omega - i\Omega\langle\sigma_1\rangle, \tag{C5}$$

where we used $\sigma_1\sigma_3 = -i\sigma_2$, $\sigma_i\sigma_i = I$, and $c^2 - s^2 = \Delta_{AL}/(2\Omega)$.

The other two equations for $\langle\dot{\sigma}_2\rangle$ and $\langle\dot{\sigma}_3\rangle$ can be got following similar steps. So the following Bloch component equations are obtained (assume $\gamma_0 = \gamma_+$ for simplicity):

$$\langle\dot{\sigma}_1\rangle = -\Delta_{AL}\langle\sigma_2\rangle - \frac{1}{T_u}\langle\sigma_1\rangle + V,$$

$$\langle\dot{\sigma}_2\rangle = \Delta_{AL}\langle\sigma_1\rangle + 2\epsilon\langle\sigma_3\rangle - \frac{1}{T_v}\langle\sigma_2\rangle,$$

$$\langle\dot{\sigma}_3\rangle = -2\epsilon\langle\sigma_2\rangle - \frac{1}{T_w}(\langle\sigma_3\rangle + 1) + V\langle\sigma_1\rangle. \tag{C6}$$

Here, $1/T_{u,v} = [c^2(1+s^2)\gamma_+ + s^4\gamma_- + 4\gamma_p]/2 \mp c^2 s^2(\gamma_+ - \gamma_-)/2$, $1/T_w = c^2(1+s^2)\gamma_+ + s^4\gamma_-$, and $V = (\gamma_+ - \gamma_-)cs^3$. T_u and T_v reduce to the transverse dephasing time and T_w reduces to the longitudinal dephasing time in ordinary vacuum if we set $\gamma_+ = \gamma_-$. V is a novel vacuum structure term arising purely from the jump structure of the electromagnetic vacuum.

The Bloch component equations can be written in vector form

$$\dot{\boldsymbol{\rho}} = \boldsymbol{\Omega} \times \boldsymbol{\rho} - \Gamma_{\boldsymbol{\rho}} + \mathbf{C}, \tag{C7}$$

where

$$\boldsymbol{\rho} = (\langle\sigma_1\rangle, \langle\sigma_2\rangle, \langle\sigma_3\rangle) = (u, v, w), \quad \boldsymbol{\Omega} = (-2\epsilon, 0, \Delta_{AL}),$$

$$\Gamma_{\boldsymbol{\rho}} = (u/T_u, v/T_v, w/T_w), \quad \mathbf{C} = (V, 0, -1/T_w + Vu).$$

[1] S. John, Phys. Rev. Lett. **53**, 2169 (1984).
[2] S. John, Phys. Rev. Lett. **58**, 2486 (1987).
[3] E. Yablonovitch, Phys. Rev. Lett. **58**, 2059 (1987).
[4] A. Chutinan, S. John, and O. Toader, Phys. Rev. Lett. **90**, 123901 (2003).
[5] A. Chutinan and S. John, Phys. Rev. E **71**, 026605 (2005).
[6] A. Chutinan and S. John, Phys. Rev. B **72**, 161316 (2005).
[7] A. Chutinan and S. John, Opt. Express **14**, 1266 (2006).

[8] T. Y. M. Chan and S. John, Phys. Rev. A **78**, 033812 (2008).
[9] R. Wang and S. John, Phys. Rev. A **70**, 043805 (2004).
[10] S. John and R. Wang, Photonics Nanostruct. Fundam. Appl. **2**, 137 (2004).
[11] X. Ma and S. John, Phys. Rev. Lett. (to be published).
[12] T. Yoshie, A. Scherer, J. Hendrickson, G. Khitrova, H. M. Gibbs, G. Rupper, C. Ell, O. B. Shchekin, and D. G. Deppe, Nature (London) **432**, 200 (2004).
[13] J. P. Reithmaier, G. Sek, A. Loffler, C. Hofmann, S. Kuhn, S. Reitzenstein, L. V. Keldysh, V. D. Kulakovskii, T. L. Reinecke, and A. Forchel, Nature (London) **432**, 197 (2004).
[14] E. Peter, P. Senellart, D. Martrou, A. Lemaitre, J. Hours, J. M. Gerard, and J. Bloch, Phys. Rev. Lett. **95**, 067401 (2005).
[15] X. Xu, B. Sun, P. R. Berman, D. G. Steel, A. S. Bracker, D. Gammon, and L. J. Sham, Science **317**, 929 (2007).
[16] A. N. Vamivakas, Y. Zhao, C. Lu, and M. Atature, Nat. Phys. **5**, 198 (2009).
[17] E. B. Flagg, A. Muller, J. W. Robertson, S. Founta, D. G. Deppe, M. Xiao, W. Ma, G. J. Salamo, and C. K. Shih, Nat. Phys. **5**, 203 (2009).
[18] I. I. Rabi, Phys. Rev. **51**, 652 (1937).
[19] L. Allen and J. H. Eberly, *Optical Resonance and Two-level Atoms* (Wiley, New York, 1975).
[20] S. L. McCall and E. L. Hahn, Phys. Rev. Lett. **18**, 908 (1967).
[21] E. B. Treacy, Phys. Lett. A **27**, 421 (1968).
[22] M. M. T. Loy, Phys. Rev. Lett. **32**, 814 (1974).
[23] B. R. Mollow, Phys. Rev. **188**, 1969 (1969).
[24] O. Toader, S. John, and K. Busch, Opt. Express **8**, 217 (2001).
[25] S. John and J. Wang, Phys. Rev. Lett. **64**, 2418 (1990).
[26] S. John and T. Quang, Phys. Rev. Lett. **74**, 3419 (1995).
[27] M. Florescu and S. John, Phys. Rev. A **69**, 053810 (2004).
[28] M. Florescu and S. John, Phys. Rev. A **64**, 033801 (2001).
[29] S. John and M. Florescu, J. Opt. A, Pure Appl. Opt. **3**, S103 (2001).
[30] S. John and T. Quang, Phys. Rev. Lett. **78**, 1888 (1997).
[31] M. Lewenstein and T. W. Mossberg, Phys. Rev. A **37**, 2048 (1988).
[32] T. W. Mossberg and M. Lewenstein, J. Opt. Soc. Am. B **10**, 340 (1993).
[33] D. Vujic and S. John, Phys. Rev. A **76**, 063814 (2007).
[34] N. V. Vitanov, T. Halfmann, B. W. Shore, and K. Bergmann, Annu. Rev. Phys. Chem. **52**, 763 (2001).
[35] S. M. Hamadani, A. T. Mattick, N. A. Kurnit, and A. Javan, Appl. Phys. Lett. **27**, 21 (1975).
[36] B. Broers, H. B. van Linden van den Heuvell, and L. D. Noordam, Phys. Rev. Lett. **69**, 2062 (1992).
[37] D. Goswami and W. S. Warren, Phys. Rev. A **50**, 5190 (1994).
[38] M. E. Crenshaw, M. Scalora, and C. M. Bowden, Phys. Rev. Lett. **68**, 911 (1992).
[39] M. E. Crenshaw and C. M. Bowden, Phys. Rev. Lett. **69**, 3475 (1992).
[40] J. Lourtioz, H. Benisty, V. Berger, J. Gerard, D. Maystre, and A. Tchelnokov, *Photonic Crystals* (Springer, New York, 1999).
[41] H. Benisty, J. Lourtioz, A. Chelnokov, S. Combrie, and X. Checoury, Proc. IEEE **94**, 997 (2006).
[42] S. Hughes and H. Kamada, Phys. Rev. B **70**, 195313 (2004).
[43] H. Ee, H. Park, L. A. Eldada, and E. Lee, *Optoelectronic Integrated Circuits XI* (SPIE, San Jose, CA, 2009), Vol. 7219, p. 72190G.
[44] A. Mostafazadeh, *Dynamical Invariants, Adiabatic Approximation, and the Geometric Phase* (Nova Science Publishers, Huntington, NY, 2001).
[45] A. Mostafazadeh, Phys. Lett. A **320**, 375 (2004).
[46] K. Shenai, R. S. Scott, and B. J. Baliga, IEEE Trans. Electron Devices **36**, 1811 (1989).
[47] L. C. Andreani, G. Panzarini, and J. M. Gerard, Phys. Rev. B **60**, 13276 (1999).
[48] T. H. Stievater, X. Li, D. G. Steel, D. Gammon, D. S. Katzer, D. Park, C. Piermarocchi, and L. J. Sham, Phys. Rev. Lett. **87**, 133603 (2001).
[49] V. S. Letokhov, Sov. Phys. JETP **29**, 221 (1969).
[50] C. Cohen-Tannoudji, *Atom-Photon Interactions—Basic Processes and Applications* (Wiley, New York, 1992).